# Chemical and physical erosion rhythms of the West African Cenozoic morphogenesis: The Ar-39-(40) Ar dating of supergene K-Mn oxides

Anicet Beauvais, Gilles Ruffet, Olivier Hénocque, Fabrice Colin

# Chemical and physical erosion rhythms of the West African Cenozoic morphogenesis: $^{39}Ar$-$^{40}Ar$ dating of supergene K-Mn oxides

Anicet Beauvais [a*], Gilles Ruffet [b], Olivier Hénocque [a], Fabrice Colin [c]

[a] *CEREGE (Centre Européen de Recherche et d'Enseignement de Géosciences de l'Environnement), Aix-Marseille Université, CNRS, IRD, CdF, BP 80, 13545 Aix-en-Provence Cedex 4, France*

[b] *Géosciences Rennes, Université de Rennes 1, CNRS, CAREN, 35042 Rennes Cedex, France*

[c] *IRD (Institut de Recherche pour le Développement), BP A5, 98848 Nouméa, Nouvelle-Calédonie*

[*] Corresponding author: beauvais@cerege.fr (Tel/Fax: 33 4 42 97 17 73/ 33 4 42 97 15 95)

## Abstract

Chemical weathering and mechanical erosion are first order processes of long-term tropical morphogenesis, which is still poorly deciphered for lack of time constraints. We address this issue by laser-probe $^{39}Ar$-$^{40}Ar$ dating of generations of cryptomelane [$K_{1-2}Mn_8O_{16}$, $nH_2O$] from the manganese ore deposit of Tambao in northern Burkina Faso. This Mn deposit results from the supergene weathering of carbonate and silicate Mn-protores underneath lateritic palaeolandsurfaces. It consists of an upper cryptomelane-rich domain, and a lower domain where pyrolusite ($\beta$-$MnO_2$) is the dominant Mn-oxide. The oldest $^{39}Ar$-$^{40}Ar$ ages (59-45 Ma) are obtained on surface outcrops while the youngest ones characterize deep oxidation fronts (3.4-2.9 Ma). Apparent correlations of $^{39}Ar$-$^{40}Ar$ age groups with $\delta^{18}O$ and eustatic curves allow definition of the different stages of morphogenesis. Paleocene-Eocene ages (59-45 Ma), bracket a greenhouse period propitious to bauxitic weathering. The lack of significant ages between ca. 45 Ma and 29 Ma characterizes a period dominated by mechanical erosion, during which detrital sediments including lateritic materials were accumulated in intracratonic basins allowing the exhumation of a new lateritic landsurface. Two major weathering periods separated by a second erosion episode (24-18 Ma) are also depicted at the end of Oligocene (29-24 Ma) and lower to mid-Miocene (18-11.5 Ma) in the upper domain, during which newly shaped landsurfaces conspicuously weathered. The shorter weathering and erosion episodes recorded in the lower domain from ca 18 Ma to ca 2.9 Ma led to the final geomorphic changes that were conducive to the formation of glacis. The preservation of old cryptomelane (59-45 Ma) in the upper part of the ore deposit indicates a Cenozoic denudation limited to the erosion of previous bauxites, and partly, of ferricretes.



*Keywords* – Laser-probe $^{39}Ar$-$^{40}Ar$ dating, Cryptomelane, Lateritic paleolandsurface, Cenozoic denudation, Long-term morphogenesis, West Africa

## 1. Introduction

Most lateritic deposits and tropical soils result from long-term meteoric weathering of the lithosphere and are still widespread on the Earth surface, especially throughout the tropical belt [*Pedro*, 1968; *Nahon*, 1991]. Following Gondwana break-up, physical and chemical processes driven by epeirogeny and climate led to the development of tens of meters of thick weathering mantles including bauxites and ferricretes, which are preserved on stepped relicts of abandoned planation surfaces and pediplains [*Millot*, 1983; *Aleva*, 1984; *Bardossy and Aleva*, 1990; *Nahon et al*., 1992; *Tardy and Roquin*, 1998; *Chevillotte et al.*, 2006]. These lateritic paleosurface relicts result from the combination of long-term weathering, incision and erosion processes [*King*, 1967; *Partridge and Maud*, 1987]. According to the synthetic morphogenetic sequence described in West Africa [*Vogt*, 1959; *Michel*, 1973; *Grandin*, 1976; *Boulangé and Millot*, 1988; *Thomas*, 1994], the highest surfaces carrying bauxite dominate landsurfaces with different generations of ferricrete (Figure 1). Manganese ore deposits may also develop within specific rock's weathering mantles. Below the bauxitic paleosurface, the intermediate ferricrete-capped relief dominates three pediments (Figure 1) so called lateritic glacis in West Africa [*Thomas*, 1994], and defined as high, middle and low glacis. The term glacis defines a gently inclined surface carrying detrital lateritic and bedrock materials.

The age determination of the paleosurfaces and their lateritic weathering remains a critical issue in estimating the erosion rates and constraining the long-term tropical morphogenesis and the evolution of continental palaeoclimates. A relative chronology of the lateritic landsurfaces was assessed by examining the height differences between the landsurfaces and the geochemical composition of the associated lateritic materials that allowed a first estimation of the erosion rates [*Tardy and Roquin*, 1998]. However, better-constrained ages of past chemical weathering and mechanical erosion periods can be obtained by performing $^{39}Ar$-$^{40}Ar$ laser-probe dating of K-Mn oxides in supergene manganese ore

deposits that constitute a perfect alternative to the apatite fission track approach [*Gunnell*, 2003] to constrain the Cenozoic cratonic denudation for different time spans.

Previous geochronological studies proved the usefulness of K-Ar and $^{39}$Ar-$^{40}$Ar methods to date potassium-rich supergene minerals such as cryptomelane [*Vasconcelos et al*, 1992, 1994; *Lippolt and Hautmann*, 1995; *Ruffet et al.*, 1996; *Hénocque et al.*, 1998]. This K-Mn oxide is believed to reflect strong lateritic weathering conditions [*Parc et al.*, 1989], and it is ubiquitous in numerous supergene manganese ore deposits [*Nahon et al.*, 1984; *Beauvais et al.*, 1987; *Roy*, 1981, 1988; *Dasgupta et al.*, 1992; *Ostwald*, 1992; *Pracejus and Bolton*, 1992; *Varentsov*, 1996]. The Tambao Mn ore deposit in northern Burkina Faso is clearly integrated in the continental scale geomorphological sequence (Figure 1) and its high cryptomelane content [*Perseil and Grandin*, 1978] motivated $^{39}$Ar-$^{40}$Ar geochronological investigations. $^{39}$Ar-$^{40}$Ar-laser method was first performed on two Mn-rich botryoidal concretions [*Henocque et al.*, 1998] that showed an episode of cryptomelane formation between 44.5 and 50 Ma. Later, $^{39}$Ar-$^{40}$Ar age groups of 59-56 Ma, 47-44 Ma and 27-24 Ma were obtained on seven samples of manganiferous pisolites deriving from a massive Mn-crust [*Colin et al.*, 2005]. These previous results allowed linking of the formation of surface Mn-crusts and pisolites to the Paleogene bauxitic period. In this paper we investigate many more samples from drill cores to better characterize the successive stages of the Mn-ore deposit formation that may usefully document the long-term (Paleogene + Neogene) morphogenesis and denudation.

## 2. Material, sampling and analytical methods

Cryptomelane occurs in single or multiple generations associated with other Mn-oxides [*Beauvais et al.*, 1987]. This is the K-rich end member of the hollandite Mn-oxide group with a general formula, $A_{1\text{-}2}B_8O_{16}$, $nH_2O$ (with A = $K^+$, $Ba^{2+}$, $Na^+$, $Pb^{2+}$ and B = $Mn^{4+}$, $Mn^{2+}$, $Fe^{3+}$, $Al^{3+}$), and a tunnel structure made by double chains of $MnO_6$ octahedra [*Burns and Burns*,

1979; *Turner and Buseck*, 1979]. Large cations of the A site counterbalance the charge deficit due to the Mn oxidation states and the other cations of the B site. The cryptomelane structure increases its potassium and argon retentiveness, and thus its suitability for K-Ar and $^{39}$Ar-$^{40}$Ar geochronological investigations [*Vasconcelos et al.*, 1992, 1994].

The first applications of the K-Ar dating method to cryptomelane were very promising despite problems of phase mixing and difficulties for extracting pure samples [*Chukhrov et a*l., 1966; *Yashvili and Gukasyan*, 1974; *Varentsov and Golovin*, 1987; *Segev et al.*, 1991]. The small quantities required for $^{39}$Ar-$^{40}$Ar-laser-probe dating reduce the mixing risks [*Ruffet et al*., 1996], which are further lessened by a precise sampling [*Hénocque et al.*, 1998].

## 2.1. Petrography and mineralogy

Samples were taken from drill cores DD2B, DDH76-02 and DDH76-09 of 110-meter and 40-meter-length, respectively (Figures 2 and 3) and from outcrops of manganese oxide benches. DD2B, DDH76-02 and DDH76-09 cores were drilled on the high and low hills (Figure 2). The altitude of samples in the cores and at the surface of the deposit is calculated to allow comparisons and to define relations with landsurface processes.

Polished thin sections of samples were observed with an optical microscope (Leica DMRXP) while scanning electron microscopy (SEM) was used for subsample investigations.

Manganese oxides were characterized by X-ray diffraction, using a Philips PW 1710 diffractometer with a Cu-tube anode ($k\alpha1 = 1.78896$; $k\alpha2 = 1.79285$) to avoid fluorescence effects. Major chemical elements were measured out using ICP-OES.

When several cryptomelane generations occurred in a same sample, subsamples were extracted and identified with a capital letter (BF96-327-A and BF96-327-B) or a two-digit number (01, 02, 03, etc). The subsamples selected for $^{39}$Ar-$^{40}$Ar dating were labeled with a small letter added to the sample number (e.g., BF96-632-a1 and BF96-632-f2).

## 2.2. $^{39}$Ar-$^{40}$Ar analysis

Samples selected for $^{39}$Ar-$^{40}$Ar dating were hand picked from 0.5 mm thin slabs cut from petrographic samples. They were wrapped in Al-foil to form small packets, which were stacked into a column within which packets of flux monitors were inserted every 8 to 10 samples. This configuration allows determination of the vertical flux gradient with a precision as low as ± 0.2%. Samples were irradiated in the 5C position of the McMaster reactor (Hamilton, Canada) together with biotite monitor Bern4B (17.25 Ma) [*Hall et al.*, 1984], with amphibole monitor Zartman Hb3gr (1072 Ma) [*Zartman*, 1964; *Turner*, 1971; *Roddick*, 1983], or with sanidine monitor Draz (24.99 Ma) [*Wijbrans*, pers. com.]. Because the sample age was unknown, 4 to 70 hours irradiations were tested [*Hénocque et al.*, 1998], 25 hours being the most suitable.

A VG® 3600 mass spectrometer equipped with a Daly® detector was used for analyses. Each static measurement of argon isotopes corresponds to 11 peak hopping scans. Backgrounds of the extraction and purification line were measured every first or third step and subtracted from each argon isotope of the subsequent gas fractions. Typical blank values were included in the ranges $3.2\times10^{-12}$<M/e40<$4.8\times10^{-13}$, $7.4\times10^{-14}$<M/e39<$4.6\times10^{-15}$, $6.6\times10^{-14}$<M/e38<$3.5\times10^{-16}$, $1.3\times10^{-13}$<M/e37<$1.7\times10^{-14}$ and $7.6\times10^{-14}$<M/e36<$2.1\times10^{-15}$ cm$^3$ STP. All isotopic measurements were corrected for K, Ca and Cl isotopic interferences, mass discrimination and atmospheric argon contaminations. Three consecutive steps accounting for 70% of the total $^{39}$Ar released define a plateau age and the individual age fractions must agree within 2σ error bars of the "integrated" age of the plateau segment. Pseudo-plateau ages can be calculated, however, with less than 70% of the $^{39}Ar_K$ released. All errors are quoted at the 1σ level and do not account for $^{40}Ar^*/^{39}Ar_K$ ratio and monitor age uncertainty, which is included in the calculation of the plateau age error.

## 3. Geographical, geomorphological and geological setting

The Tambao Mn ore deposit is located in North Burkina Faso (14°47'N, 0°04'E) in the sub-sahelian area close to a continental sedimentary basin (Figure 2). The mean annual rainfall is 375 mm. The vegetation is composed of a grassy steppe alternating with forest patches along river drainage axes. The Mn-ore deposit is composed of two hills corresponding to lateritic landsurface relicts.

### 3.1. Distribution and characterization of lateritic landsurfaces

Four major landsurfaces are observed around Tambao (Figures 1 and 2). The highest one is identified on the high hill between 353 and 325 meters elevation corresponding to a relict of the intermediate landsurface [*Grandin*, 1976], which bears ferricrete and/or Fe-Mn and Mn pisolitic crusts [*Colin et al*., 2005]. The second landsurface observed between 325 and 300 m on the highest hillslope corresponds to the high glacis, which is characterized by a quartzose ferricrete incorporating reworked manganiferous and ferruginous pebbles originating from the upper landsurface. The low hill also shows intermediate Fe-Mn crust relicts, the high glacis being mainly represented between 325 and 300 m with a quartzose ferricrete (Figure 2). Two lower landsurfaces are observed in the surrounding plain at about 300-280 m and < 280 m corresponding to the middle- and low glacis, respectively. The former bears a ferricrete, while the second is a sandy erosion surface.

### 3.2. Parent rocks and protores

Long-term lateritic weathering of a complex parent rocks assemblage has produced a 70 to 80 meter thick supergene manganese ore deposit (Figures 2 and 3). The Tambao Mn-

deposit hosts a reserve of about 15 Mt of manganese-ore with an MnO content of 75 wt.% [*Boulanger and Sanguinetti*, 1970]. Four layers of manganese ores developed from weathered Birimian (Paleoproterozoic age) metavolcanic and metasedimentary rocks (Figure 2), composed of schist, micaschist, tuff, carbonate and quartzite [*Delfour*, 1963; *Grandin*, 1976]. Metamorphism of the Birimian rocks is related to syn- and post-tectonic granite and granodiorite intrusions [*Picot and Trinquard*, 1969]. The metamorphic carbonates and tuffs are the main protores of the Mn deposit reflecting the mining quality of the ore [*Boulanger and Sanguinetti*, 1970; *Collins et al.*, 1971], which consists of a high grade carbonate ore with hausmannite ($Mn_3O_4$), a rhodochrosite-rich carbonate ore and a low grade carbonate ore containing kutnahorite ([Ca, Mg, Mn] $CO_3$). About 70% of the Mn ore derives from the weathering of rhodochrosite (Figure 3) [*Picot and Trinquard*, 1969] and 30% from the weathering of spessartine rich quartzite [*Perseil and Grandin*, 1978].

## 4. Weathering and oxidation of protores

### 4.1. Petrography

In drill core DD2B, at altitudes ranging from 241 and 265 m (Figure 3), the parent rock is a very heterogeneous carbonate protore characterized by a ribbon pink carbonate matrix embedding thin beds (0.1-1 m thick) of manganese oxides grains, which preserve the ribbon structure. The transition between the protore and the oxidized Mn-ore is thin and partly masked by a small albitite sill in drill DD-2B (Figure 3). Between 270 and 345 m (Figure 3), the parent rock is directly replaced by the oxidized manganese ore (layer III), which also partially preserves primary structures (folds and schistosity). The top of the core (345 m) is mostly composed of detrital lateritic material. The drill core also cut across more or less weathered granite and kaolinite-rich layers between 275 and 335 m (Figure 3). The oxidation

of the manganese carbonate protore induced a large porosity in which botryoidal manganese oxide aggregates developed [*Hénocque et al.*, 1998].

The drill core DDH76-02 allows exploration of layers I, II and III (Figure 3). The parent rock was not reached by the drill core but could be directly observed from outcrops. Successions of manganese-rich and manganese-poor layers (10 cm thick) characterize the quartzite formation. The manganese oxides layers deriving from the weathering of Mn-garnet (spessartine) rich quartzite are thinner. Between 270 and 350 m, the manganese oxides present various aspects, porous and light and/or massive and heavy with many botryoidal concretions. In this core, manganese oxide layers alternate with weathered schist between 280 and 285 m, 300 and 310 m, and at 330 m, and with weathered granite between 315 and 325 m and at 340 m, occurring as a quartz rich kaolinitic saprolite (Figure 3). The drill core DDH76-09 allows investigation of layer IV, between 305 and 315 m, the lower part of the core being composed of weathered schist between 290 and 305 m (Figure 3).

### 4.2. Mineralogy and bulk chemistry

Rhodochrosite ($MnCO_3$) and/or kutnahorite ($CaMn(CO_3)_2$) are the predominant primary minerals of the carbonate protore, with small amounts of opaque minerals such as hausmanite ($Mn^{2+}Mn^{3+}{}_2O_4$) and hetaerolite ($ZnMn_2O_4$), aligned parallel to the rock schistosity. Transmitted light microscopy also reveals tephroite ($Mn_2SiO_4$) and rhodonite ($MnSiO_3$), which are also oriented parallel to the rock schistosity. The weathering is characterized by *in situ* transformation of rhodochrosite, hausmannite and tephroite into manganite (MnOOH), todorokite ($[Mn^{2+}, Mg,Ca,Ba,Na,K]_2[ Mn^{4+},Mn^{3+}]_7O_{12}. 3H_2O$), and pyrolusite ($\beta$-$MnO_2$), while spessartine ($Mn_3Al_2[SiO_4]_3$) and rhodonite weathered into lithiophorite ($[Al,Li]MnO_2[OH]_2$).

The manganese oxide ore of layer II developed according to three stages. Spessartine was replaced by lithiophorite. The voids resulting from the dissolution of quartz, kaolinite and

pyrolusite are filled with cryptocrystalline cryptomelane. The manganese oxides were transformed into well-crystallized thin needles of cryptomelane (Figure 4).

The weathering of the carbonate protore leads to the formation of manganite, pyrolusite and nsutite ($\gamma$-$MnO_2$) associated with todorokite. During a first weathering stage cryptomelane occurs only in small veinlets (Figure 5a). Pyrolusite exhibits large prismatic crystals with a characteristic fracture pattern. It is transformed into cryptomelane matrices in the upper part of the deposit (Figure 5b) as indicated by the increase of $K_2O$ (Figure 6). Multiple cryptomelane generations also occur into botryoidal aggregates (Figure 5c).

### 4.3. Potassium sources for cryptomelane

Because the Mn-protores do not contain much potassium (Figure 6), sources of potassium are found in the surrounding rocks of the basement and the metavolcanic and metasedimentary rocks of the Birimian Supergroup (schists, granites, granodiorites and migmatites). Large amounts of potassium can be also trapped with clay-organic molecules and also into detrital minerals like illite and micas in the upper soil horizons. The release of potassium in $Mn^{2+}$-rich solutions during the weathering of K-phyllosilicates into kaolinite can contribute to the formation of cryptomelane [*Parc et al.*, 1989]. The depletion of Mn and K from the upper part of the deposit was also observed during the late transformation of the massive Mn-crust into pisolitic formation, this process being contemporaneous of the major Eocene bauxitic period [*Colin et al.*, 2005]. Bauxites in the tropics formed under humid climate with a dense vegetation cover that suggests high amounts of organic acids in solutions, which can dissolve K-phyllosilicates and previously formed Mn- and K-Mn oxides, with the release of K and Mn contributing to new cryptomelane growth in oxygenated zones of the deposit.

## 5. Geochronological investigation

### 5.1. $^{39}$Ar-$^{40}$Ar age spectra configurations

The stability of the K-Ar isotopic system within cryptomelane structure mainly depends on geochemical interactions with fluids. The retentivity of argon and potassium isotopes in cryptomelane has been investigated [*Lippolt et Hautmann*, 1995; *Vasconcelos et al*., 1995; *Vasconcelos*, 1999]. The various configurations of the age spectra obtained during $^{39}$Ar-$^{40}$Ar analyses have been discussed [*Vasconcelos et al*., 1995; *Ruffet et al*., 1996; *Hénocque et al*., 1998; *Hautmann et Lippolt*, 2000] that allowed definition of three types of age spectra improving the $^{39}$Ar-$^{40}$Ar data interpretations.

Type 1 "staircase" age spectra are characterized by a rapid increase of the ages in the low temperature steps followed by a rather flat segment that allows definition of a plateau age (Figure 7a). These age spectra however suggest $^{40}$Ar* losses linked to a younger weathering "episode" that could have altered the peripheral intra crystalline retention sites or induced secondary growth.

Type 2 "hump-shape" age spectra often show concordant "young" ages in the low and high temperature steps and "old" ages in the intermediate degassing temperatures (Figure 7b) indicating mixing of different manganese oxide generations. The low and high temperature ages are maximum estimates of the youngest generation true age, whereas the intermediate temperature ages are underestimates of the oldest generation true age.

Type 3 age spectra exhibit an irregular shape with a "staircase" in the low temperature steps, the ages reaching a "maximum" followed by a decrease in the second part of the spectra up to the fusion of the mineral (Figure 7c). Mixing of different mineral generations or $^{39}$Ar recoil during irradiation complicate the interpretation of these age spectra [*Turner and Cadogan*, 1974], although apparently significant ages can be often obtained.

285

286 **5.2. $^{39}$Ar-$^{40}$Ar results**

287

288 The results were subdivided into three groups according to the altitude of the

289 cryptomelane samples (Figures 8, 9, and 10). $^{39}$Ar-$^{40}$Ar runs are available as an online dataset.

290

291 5.2.1. First group of age spectra

292

293 The first group of age spectra corresponds to cryptomelane samples taken between the

294 groundsurface and -17 m depth, i.e., between altitudes of 342 to 325 m that are included

295 within the topographic boundaries of the intermediate landsurface (Figures 2 and 3). Fourteen

296 age spectra obtained on ten samples exhibit 4 Type 1 (staircase) and 9 Type 2 (hump) shapes

297 (Figure 8). The oldest apparent ages (≥ 43 Ma) are obtained for outcrops samples Col3 and

298 BF96-190 (Figure 8a). Col3 was taken from outcropping layer III, at an altitude of 325 m, on

299 the northeastern slopes of the high hill. This sample is part of a cryptomelane vein crossing a

300 pyrolusite ore, similar to the ones developed at the transition between pyrolusite- and

301 cryptomelane domains in the drill core DD2B (Figure 6). BF96-190 corresponds to the

302 transition (at an altitude of 345 m) between the massive ore (Layer III) and the pisolitic crusts

303 [*Colin et al.*, 2005] and it is the oldest one with a pseudo plateau age at 59.0 ± 0.1 Ma (45.2%

304 $^{39}$Ar released). The age spectrum however exhibits a staircase shape with low temperature

305 apparent ages at ca 46.5 Ma indicating apparent $^{40}$Ar* loss due to peripheral perturbations

306 and/or growth of a younger cryptomelane generation.

307 The four sub-samples of Col3 (b to e) are characterized by hump-shaped age spectra

308 (Figure 8a). Col3b and Col3e show the oldest pseudo plateau ages at 48.9 ± 0.1 Ma and 49.9

309 ± 0.2 Ma, respectively. Col3c shows a pseudo-plateau age at 44.9 ± 0.3 Ma, and Col3d is

310 characterized by an apparent age at 46.3 ± 0.2 Ma (58% $^{39}$Ar released). The spectra show

311 "maximum ages" as young as the magnitude of the hump is high that could indicate a mixing
312 of two cryptomelane generations. The ages (ca. 45-50 Ma) for Col3 are however concordant
313 with the ones previously obtained for two cryptomelane concretions [*Hénocque et al.*, 1998].
314 Drill core samples yield systematically younger ages than outcrop and surface samples
315 (Figures 8b and 8c). Samples BF96-202c3, 211, 215 and 218-a of the upper part of drill core
316 DDH-76-02 (342-330 m) are characterized by hump shaped age spectra with maximum
317 apparent ages between 34-40 Ma in the intermediate temperature steps (Figure 8b). BF96-
318 218a and 215 exhibit small concordant pseudo-plateau ages in the low temperature steps at
319 24.6 ± 0.8 Ma and 24.1 ± 1.2 Ma, respectively (Figure 8b). BF96-229 is a small cryptomelane
320 vein in the weathered granite between layers II and III in drill core DDH-76-02 (326 m) and it
321 displays a plateau age at 17.8 ± 0.1 Ma with 64.1% $^{39}$Ar released (Figure 8b). The staircase
322 age spectrum of sample BF96-104 (327 m in Drill core DD2B) also allows definition of a
323 plateau age at 17.4 ± 0.2 Ma with 87% $^{39}$Ar released (Figure 8c). Age spectra of samples
324 BF96-107 and BF96-108a (upper part of drill core DD-2B) display "old" and "young"
325 apparent ages in the low to intermediate temperature steps at 25.6 ± 0.4 Ma (20% of the total
326 $^{39}$Ar released) and 17.7 ± 0.4 Ma (23% of the total $^{39}$Ar released), respectively, which are
327 nearly concordant with the fusion step apparent age (Figure 8c). The age-frequency diagram
328 (Figure 8d) reveals three major age intervals, 35-50, 23-27 and 15-18 Ma.
329
330 5.2.2. Second group of age spectra
331
332 The second group of age spectra consists of samples taken at depths ranging from -18 to -
333 42 m that correspond to the lower part of the cryptomelane domain at altitudes of 324 to 300
334 m (Figure 3), i.e., the topographic boundaries of the high glacis landsurface (Figure 2). This
335 group of 19 samples (Figure 9) shows 24 age spectra with 6 Type 1 (staircase) shapes, 17
336 Type 2 (hump) shapes, and 1 Type 3 shape (BF96-101-b2). Samples of the high hill cores

337 (DD2B and DDH76-02) were taken within the layer III between 325 and 320 m (BF96-97,
338 98, 101 and 102) and between 315 and 300 m (BF96-251, 256, 96, 260, 94 and 273). Samples
339 of the low hill core were taken between 315 and 313 m (BF96-559, 561 and 563) and between
340 309 and 300 m (BF96-571-02, 575-b and 577) (Figure 3). Sample Col1 and BF93-632-f2 are
341 outcrop and surface sample, at altitudes of 320 m and 307 m, respectively.

342 Col1 is cryptomelane developing from metasomatism of pyrolusite (Figure 5b). Col1
343 duplicates irradiated for 5 and 70 hours yielded very similar hump shape age spectra (Figure
344 9a) indicating no $^{39}$Ar recoil during irradiation. The two age spectra show nearly concordant
345 maximum ages in the range 45.3 ± 0.4 - 44.4 ± 0.1 Ma while one obviously shows a small
346 pseudo-plateau age at 27.3 ± 0.7 Ma derived from six concordant steps at low temperature (5
347 to 15% of the total $^{39}$Ar released) that is also concordant with high temperature ages (Figure
348 9a). BF93-632 is a hollandite concretion sampled underneath the high glacis ferricrete at an
349 altitude of 307 m. A sub-sample (BF96-632-a1) yields an interesting hump-shaped age
350 spectrum with concordant low and high temperature ages at ca 16 Ma (Figure 9a). A second
351 sub-sample (BF96-632-f2) is characterized by a staircase age spectrum with low temperature
352 ages at ca. 16 Ma (Figure 9a), and an intermediate to high temperature pseudo-plateau age at
353 36.2 ± 0.2 Ma (46.3% of the total $^{39}$Ar released).
354 Samples of DD2B core are characterized by plateau ages calculated from staircase and hump-
355 shaped age spectra around 24 Ma (Figures 9b) and at 14.9 ± 0.1 Ma and 17.1 ± 0.1 Ma
356 (Figure 9c). An older plateau age was also calculated at 28.8 ± 0.1 Ma (BF96-251) while four
357 younger plateau ages are evident between 11.5 ± 0.2 Ma and 14.6 ± 0.3 Ma for DD76-02 core
358 samples (Figure 9d). Sample BF96-260 with younger apparent ages (ca 21-22Ma) exhibits a
359 clear hump shape that does not allow plateau age calculation (Figure 9d).
360 Samples of DDH76-09 core provided plateau ages at 27.1 ± 0.3 Ma, and two younger at ca.
361 24-25 Ma (Figure 9e). One sample (BF96-577) at an altitude of 304 m is characterized by a

unique "older" age at 36.3 Ma (Figure 9f) that is comparable with the intermediate to high temperature age of BF96-632-f2 (Figure 8a). The age frequency diagram reveals four age and/or age intervals, 12.5, 14-17, 21-25 and 27-29 Ma (Figure 9g) all being concordant with objectively calculated pseudo-plateau and plateau ages.

5.2.3. Third group of age spectra

The third group of age spectra consists of samples mainly taken from the pyrolusite-rich core (BF96-62, 91, 93, 299, 314, 318, 322, 327, 581, 653) between depths of -42 m to -89 m corresponding to altitudes of 300 m to 253 m, which are also the topographic ranges of the two lowest glacis (Figures 2 and 3). BF96-62 is a thin cryptomelane rim around a small pyrolusite concretion in the carbonate protore of DD2B core. Sample BF96-653 is a fragment of a cryptomelane vein crossing the exhumed schist saprolite of the low glacis. This third group includes 11 age spectra with 5 staircase and 6 hump shapes that allowed the calculation of 7 pseudo-plateau ages lower than 20 Ma (Figure 10).

Large error bars shown by some age spectra (BF96-62-03, BF96-91 and BF96-322) characterize the very low $K_2O$ content of these samples (e.g., 0.2 wt.% for BF96-91). Samples BF96-93 and BF96-299 of the high hill cores display plateau ages at 11.5 ± 0.1 Ma and 18.3 ± 0.3 Ma, respectively (Figures 10a and 10b). The age spectrum of BF96-581 at 293 m altitude yields older apparent ages at ca. 24 Ma, which are concordant with the plateau ages obtained upper for samples BF96-561-02, 563-02 and 575-b (Figure 9e).

Three plateau ages were also calculated for samples BF96-653, BF96-314, BF96-318 at 5.8 ± 0.1 Ma, 6.5 ± 0.1 and 7.2 ± 0.1 Ma, respectively (Figures 10a and 10b). The hump shaped age spectrum of BF96-318 exhibits concordant apparent ages at ca. 3.5-4 Ma in the low and high temperatures. The youngest ages are displayed by three samples of DDH76-02 core close to the oxidation front in the pyrolusite domain. The apparent age at ca. 3 ± 1.3 Ma

388 measured for BF96-62-03 (Figure 10a) is concordant with plateau ages at 3.4 ± 0.1 Ma
389 (80.6% $^{39}$Ar released) and 2.9 ± 0.1 Ma (74.7% $^{39}$Ar released) yielded by samples BF96-327-
390 a1 and -327-a2, respectively (Figure 10b). Ages at 5.5-7.5 Ma and ca. 3 Ma are well depicted
391 by the age frequency diagram, which also reveals ages at 11.5, 18 and 22.5 Ma (Figure 10c).
392

393 **6. $^{39}$Ar-$^{40}$Ar ages interpretation**

394
395 The oldest ages (ca. 59 Ma to ca. 45 Ma) obtained for cryptomelane of outcrop and
396 surface samples (Figure 8a) are coherent with the ages of massive Mn-crust and pisolites
397 [*Colin et al.*, 2005], and also the ages of botryoidal concretions [*Hénocque et al.*, 1998].
398 These ages indicate a sustained humid and warm paleoclimate for at least 14 Ma that could
399 represent the duration of the Eocene bauxite formation period. The age ca. 49 Ma obtained for
400 a cryptomelane at -25 m depth (Col 3) allows estimation of 2.5 m. Ma$^{-1}$ for the oxidation front
401 sinking rate between 59 and 49 Ma. However, the staircase and hump shapes of age spectra of
402 drill core samples in the highest part of layers I, II and III suggests a reactivation of
403 geochemical weathering process, and thus a rejuvenation of older minerals (Figure 8).
404 Concentric banded overgrowth structures (e.g., botryoidal) effectively result from repeated
405 geochemical mobilizations of Mn and K that led to newly formed cryptomelane generations
406 (Figure 5c). Their crystal size is so small that handpicking sampling inevitably implied
407 mixings of "old" and "young" generations characterized by hump-shaped age spectra, with
408 maximum apparent ages in the range 40-33 Ma and lower than the plateau and pseudo-plateau
409 ages of outcrop samples (Figure 8a).
410 The age spectra of the first group document two subsequent weathering episodes (Figure
411 8d). An episode at ca 27-23 Ma is obviously defined in the upper part of the cryptomelane
412 domain as shown by the diagram of plateau and pseudoplateau ages *vs*. altitude where the
413 elevation ranges of each lateritic landsurface are also represented (Figure 11a). This episode

414 was also characterized in the pisolitic crust [*Colin et al.*, 2005], where it superimposed to the
415 lateritic episode at ca. 46 Ma. The lower part of the cryptomelane domain also yields
416 reproducible pseudo-plateau and plateau ages in the range 29-24 Ma (Figure 9) that could
417 document the downward propagation of the oxidation front at an average rate of 2 m. $Ma^{-1}$.
418 Another weathering episode is depicted by low temperature ages around 18-17 Ma (Figures
419 8b, 8c and 8d). Plateau ages at 18-17 Ma were also obtained in the lower part of the
420 cryptomelane domain and for vein cryptomelane of the upper pyrolusite domain (Figures 9c
421 and 10b) that further supports the likelihood of this weathering episode.
422 The youngest ages, ca. 18 to ca. 3 Ma, document active weathering and oxidation
423 processes during the Neogene. Cryptomelane often crystallized in small veins and concretions
424 in the pyrolusite rich lower parts of the deposit indicating episodic deep circulations of
425 weathering solutions. The cryptomelane crystals are characterized by plateau ages ranging
426 between 17.8 Ma and 2.9 Ma (Figure 10), and these ages are as young as samples collected
427 close to the oxidation front (Figure11a). Figure 11a also includes $^{39}Ar$-$^{40}Ar$ ages obtained by
428 previous studies [*Henocque et al.*, 1998; *Colin et al.*, 2005]. Figure 11b shows less apparent
429 age scattering and increasing purity of analyzed parageneses with depth.
430 Although the increasing diversity of $^{39}Ar$-$^{40}Ar$ ages from the bottom to the top of the Mn-
431 deposit (Figure 11b) suggests a continuous chemical weathering for 59 Ma, five main
432 weathering periods can be differentiated. The first from ca. 59 Ma to ca. 45 Ma characterizes
433 a long weathering period, during which bauxites formed all over the tropical belt [*Bardossy*
434 *and Aleva*, 1990]. The second occurred in the range 29-24 Ma with an occurrence at 21 Ma
435 (Figure 11a), and it was well depicted in the ore deposit (Figure 9). The intermediate
436 landsurface was also deeply weathered during this major period. The three last periods are
437 characterized by short weathering episodes, 18-11.5 Ma, 7.2 -5.8 Ma and 3.4-2.9 Ma (Figure

11a), during which the three glacis were probably weathered along with recurrences between 18-11.5 Ma in the pre-existing intermediate landsurface profile (Figure 11a).

## 7. Lateritic weathering, palaeoclimates, long-term morphogenesis and denudation

Petrographical and geochemical patterns of the different lateritic landsurfaces and the height difference between the landsurfaces reflect differences in duration and intensity of weathering and erosion processes linked to contrasted paleoclimates between the Palaeogene and Neogene [*Tardy and Roquin*, 1998]. The comparison of the global $\delta^{18}O$ and eustatic curves [*Miller et al.*, 2005] with $^{39}Ar$-$^{40}Ar$ ages distribution (Figures 12a, 12b and 12c) and with the intracontinental sedimentary sequences (Figure 13a) contributes to a better understanding of the influence of Cenozoic paleoclimatic changes on West African landscapes. The age frequency histogram in Figure 12c incorporates all the results including those obtained from the previous studies [*Henocque et al.*, 1998; *Colin et al.*, 2005]. The series of $^{39}Ar$-$^{40}Ar$ ages and time intervals between these ages may document, as a surrogate for long-term paleoclimatic proxies, the major chemical weathering (warm/humid climate) and mechanical erosion (cold/dry climate) periods (Figures 12 and 13b). The altitude of dated samples and the elevation (maximum) of each planation landsurface allow estimation of average mechanical erosion rate for different time spans corresponding to the successive lateritic planation cycles.

From Paleocene (ca. 60 Ma) to middle Lutetian (ca. 45 Ma), $\delta^{18}O$ is low and the eustatic level is high [*Zachos et al.*, 2001; *Miller et al.*, 2005] (Figure 12a and 12b). The identification of marine sediment incursions between the “Continental Intercalaire” and the basal unconformity in the Iullemmeden basin, 150 km North North-East and East of Tambao (Figure 13a) indicates a maximal extension of the Saharan sound between 55 and 60 Ma in western Niger [*Petters*, 1977]. The marine sediments are mainly composed of carbonates,

464 marls, and clays dominated by sepiolite, palygorskite and attapulgite [*Millot*, 1970; *Chamley*
465 *et al*., 1988; *Ly and Anglada*, 1991] that characterize biogeochemical sedimentation. This was
466 also linked to the genesis of thick bauxitic weathering mantles inland including a differential
467 sequestration of Fe and Mn according to their respective chemical mobility.

468 Bauxites have been described on Precambrian basement and also upon the unconformity
469 (Figure 13a) between the "Continental Intercalaire" deposits and the siderolithic "Continental
470 Terminal" (CT) in the Iullemmeden basin [*Faure*, 1966; *Gavaud*, 1977; *Lang et al.*, 1990].
471 The basal sequence of CT (Upper Lutetian) is characterized by ooliths, which are also
472 interstratified within the upper siderolithic sediments [*Boudouresque et al*., 1982]. This
473 suggests that dissolved iron input originated from inland lateritic formations, whereas the
474 siderolithic detrital sediments corresponds to the mechanical erosion of lateritic weathering
475 mantles according to alternating humid and dry palaeoclimates, respectively. A ferricrete
476 specific of the intermediate surface has also been described upon the CT sediments (Figure
477 13a) of Mali and Niger [*Gavaud*, 1977; *Lang et al*., 1990]. Relicts of a similar ferricrete are
478 also present on the high hill where $^{39}$Ar-$^{40}$Ar ages of 59-45 Ma and also 29-24 Ma were
479 measured. The field observations and $^{39}$Ar-$^{40}$Ar data imply that the bauxitic and intermediate
480 ferruginous paleolandsurfaces intersected near the Tambao Mn-deposit (Figure 13a), thus
481 questioning the supposed Pliocene age of the ferricrete upon the CT sediments [*Michel*, 1973;
482 *Grandin*, 1976; *Gavaud*, 1977].

483 Biogeochemical sedimentation ceased in mid-Eocene (Lutetian) as indicated by the
484 marine sedimentary gap at the bottom of Iullemmeden [*Faure*, 1966; *Boudouresque et al*.,
485 1982] and Senegalese basins [*Ly*, 1985]. This gap might be correlated to the sea level drop
486 between ca. 34 Ma and ca. 29 Ma [*Miller et al*., 2005] (Figure 12b) that resulted from
487 Oligocene global cooling concomitant with the development of East Antarctic Ice Sheet
488 [*Salamy and Zachos*, 1999; *Zachos et al*., 2001]. These changes have induced drier climatic

conditions on continents [*Lawver et al.*, 1992], with an apogee at ca 33.5 Ma [*Kennett and Shackleton*, 1976; *Zachos et al.*, 1994, 1996; *Salamy and Zachos*, 1999; *Miller et al.*, 2005] and a persistence until the Middle Oligocene-Early Miocene [*Flower and Kennett*, 1994] as indicated by $\delta^{18}O$ increase [*Miller et al.*, 2005] (Figure12a). No significant $^{39}Ar$-$^{40}Ar$ ages were obtained in the range 45-29 Ma (Figure 12c). Following the eustatic change, the progressive sea retreat towards north and south [*Faure*, 1966] led to the incision and erosion of previous lateritic landforms. An average mechanical erosion rate of 3 m. $Ma^{-1}$ can be calculated for the period 45-29 Ma assuming an elevation of 400 m for the warped bauxitic landsurface, and the intermediate surface at 350 m (Figure 13a). At that time, continental sedimentation (siderolithic CT) could include lateritic materials eroded from early bauxitic and clay-ferruginous weathering mantles. The bauxite erosion allowed the exhumation of ferruginous materials, i.e., the formation of the ferricrete-bearing intermediate landsurface.

The next major episode of chemical weathering in Tambao occurred around 29-24 Ma (Figure 12c) corresponding with late Oligocene global warming [*Zachos et al.*, 2001] and to a relative stability of the global sea level [*Miller et al.*, 2005]. This age interval was particularly well represented in the Mn-ore deposit (Figure 9b) and could date the weathering of the recently exhumed intermediate lateritic profiles (Figures 11a and 13b) and also the formation of the older ferricrete observed upon the Iullemmeden CT sediments (Figure 13a).

Although Milankowitch glacial-interglacial cycles are well documented in the Oligocene [Retallack et al., 2004], the global Earth climate was frankly driven by a glacial-interglacial dynamic from the boundary Oligocene/Miocene [*Zachos et al.*, 2001]. The three ferruginous glacis could be formed between 24 and 3 Ma as results of the alternation of mechanical erosion and chemical weathering episodes (Figures 12 and 13b) according to low frequency climatic oscillations but higher seasonality. Except an age at ca 21 Ma, the interval 24-18 Ma could have been propitious to the mechanical erosion of the intermediate landsurface at an

514 average rate of 4 m. $Ma^{-1}$, at least partially, and to the final denudation of bauxitic remnants.
515 This major mechanical erosion episode led to the setting of the high glacis, which was
516 weathered at 18-17 Ma, 15-14.5 Ma and 12.7-11.5 Ma (Figures 11a, 12c and 13b) as
517 suggested by the increase of $\delta^{18}O$ and the relatively high sea level [*Berger and Wefer*, 1996;
518 *Miller et al.*, 2005] (Figures 12a and 12b). Coarser lateritic materials including bauxite and
519 ferricrete debris were also reworked into the newly formed high glacis landsurface that is
520 characteristic of glacis-forming processes under drier climatic conditions [*Vogt*, 1959; *Michel*,
521 1973, 1978; *Grandin*, 1976; *Boulangé and Millot*, 1988; *Thomas,* 1994]. Notice also that the
522 weathering of intermediate surface remnants could have been reactivated between 18 and 11.5
523 Ma (Figure 11a) confirming observations in other West African areas [*Beauvais et al.*, 1999,
524 2004]. The interval 11.5-7.2 Ma would correspond to the mechanical erosion of the high
525 glacis at an average rate of 6 m. $Ma^{-1}$ leading to the middle glacis emplacement before it's
526 weathering at 7.2-5.8 Ma. A short erosive episode from ca. 5.8 to 3.4 Ma at an average rate of
527 8 m. $Ma^{-1}$, which is comparable with the previously estimated erosion rate using cosmogenic
528 nuclides [*Brown et al.*, 1994], allowed emplacement of the low glacis, before this latter was
529 weathered at ca 3.4-2.9 Ma (Figure 13b).
530

531 **8. Conclusion**

532
533 $^{39}Ar$-$^{40}Ar$ ages were obtained on different cryptomelane generations sampled on outcrops
534 and drill cores in the Mn-ore deposit of Tambao (North Burkina Faso), which mainly
535 developed from the oxidation of carbonate and silicate protores. The $^{39}Ar$-$^{40}Ar$ ages were
536 compared with the variations of the global $\delta^{18}O$ and eustatic curves that documented
537 successive Cenozoic chemical weathering and mechanical erosion periods driven by the
538 alternation of warm/humid climates and cold/dry climates, respectively. The interval 59-45
539 Ma corresponds to the Eocene bauxitic period, implying that cryptomelane formed during

warm and humid periods in well-oxygenated lateritic weathering profiles. However, bauxite ferruginization and thus the starting of ferricrete individualization in the profiles characterized the end of this period, ca. 50 to ca. 45 Ma. The lack of significant measured ages from ca. 45 Ma to ca. 29 Ma corresponds to a period dominated by incision and erosion processes under drier climatic conditions, during which continental sediments started to accumulate in West African intracratonic basins. The intermediate landsurface was probably formed at the end of this period (ca. 34 to ca. 29 Ma). Then the newly exposed lateritic landsurface was further weathered between 29 and 24 Ma. This age interval could also date the ferricrete upon Iullemmeden CT sediments. The high glacis could have been shaped in the interval of 24-18 Ma, weathered around 18-17, 15-14 and 12.7-11.5 Ma, and eroded between 11.5 and 7.2 Ma, an interval propitious to the settlement of the middle glacis before this one was weathered at 7.2-5.8. The lowest glacis was shaped in the interval 5.8-3.4 Ma before the last short chemical weathering episode at 3.4-2.9 Ma. Our results allow average estimations of the oxidation front sinking rate of 2.5 m. $Ma^{-1}$ for the period 59-45 Ma against 1.5 m. $Ma^{-1}$ for the period 59-3 Ma. The average erosion rates of the successive lateritic landsurfaces would be 3 to 8 m. $Ma^{-1}$ for the period 59-3 Ma. However, persistence of lateritic landsurface relicts in the landscape, and old cryptomelane (59-45 Ma) in the upper part of the ore deposit, indicates low Cenozoic denudation rates, of the order of the height differences between the lateritic landsurfaces.

**Acknowledgments –** This is a contribution of CEREGE (UMR IRD 161), with financial support from DBT-PROSE and IRD scientific programs. We specially thank Dr. Georges Grandin and Dr. Dominique Chardon for fruitful discussions. Dominique Chardon is also gratefully acknowledged for artwork of the figure 13a.

563 # References

564

565 Aleva, G.J.J. (1984), Lateritisation, bauxitisation and cyclic landscape development in the
566 Guiana shield, in *Bauxite*, proceedings 1984 bauxite symposium, edited by L. Jacob Jr., pp.
567 111-151, AIME, New York.

568 Bardossy, G., and G.J.J. Aleva (1990), *Lateritic bauxites*, Elsevier, Amsterdam.

569 Beauvais, A., A. Melfi, D. Nahon, and J.J. Trescases (1987), Pétrologie du gisement
570 latéritique manganésifère d'Azul (Brésil), *Miner. Deposita*, *22*, 124-134.

571 Beauvais A., M. Ritz, J-C. Parisot, M. Dukhan, and C. Bantsimba (1999), Analysis of poorly
572 stratified lateritic terrains overlying a granitic bedrock in West Africa, using 2D electrical
573 resistivity tomography, *Earth Planet. Sci. Letters*, *173*, 413–424.

574 Beauvais A., M. Ritz, J-C. Parisot, C. Bantsimba, and M. Dukhan (2004), Combined ERT and
575 GPR methods for investigating two stepped lateritic weathering systems, *Geoderma*, *119*,
576 121-132.

577 Berger, W.H., and G. Wefer (1996), Expeditions into the past: Paleoceanographic studies in
578 the south Atlantic, in *The south Atlantic: present and past circulation*, edited by G. Wefer
579 et al., Springer editions.

580 Boudouresque, L., D. Dubois, J. Lang, and J. Trichet (1982), Contribution to the stratigraphy
581 and paleogeography of the western edge of the Iullemmeden basin during the upper
582 Cretaceous and Cenozoic (Niger and Mali – West Africa), *Bull. Soc. Géol. France*, *24*,
583 685-695.

584 Boulangé, B., and G. Millot (1988), La distribution des bauxites sur le craton Ouest Africain,
585 *Sci. Géol. Bulletin*, *41*, 113-123.

586 Boulanger, J.J., and H. Sanguinetti (1970), Evaluation générale du gisement de manganèse
587 de Tambao. Haute Volta, Enquêtes sur le développement minier dans le nord-est et
588 facteurs associés de transport, *Rapport n°3*, 48 pp., PNUD, Ouagadougou, Burkina Faso.

589 Brown, T.E., D.L. Bourlès, F. Colin, Z. Sanfo, G.M. Raisbeck, and F. Yiou (1994), the
590 development of iron crust lateritic systems in Burkina Faso, West Africa examined with in-
591 situ-produced cosmogenic nuclides, *Earth Planet. Sci. Letters*, *124*, 19-33.
592 Burns, R.G., and V.M. Burns (1979), Manganese oxides, in *Marine minerals*, edited by P.H.
593 Ribbe, pp. 1-46, Mineral. Soc. Am., Washington DC.
594 Chamley, H., P. Debrabant, and R. Flicoteaux (1988), Comparative evolution of the Senegal
595 and eastern central Atlantic basins, from mineralogical and geochemical investigations,
596 *Sedimentology*, *35*, 85-103.
597 Chevillotte, V., D. Chardon, A. Beauvais, P. Maurizot, and F. Colin (2006), Long-term
598 tropical morphogenesis of New Caledonia (Sothwest Pacific): importance of positive
599 epirogeny and climate change, *Geomorphology*, *81*, 361-375.
600 Chukhrov, F.V., L.L. Shanin, and L.P. Yermilov (1966), Feasibility of absolute-age
601 determination for potassium-carrying manganese minerals, *Int. Geol. Rev.*, *8*, 278-280.
602 Colin, F., A. Beauvais, G. Ruffet, and O. Hénocque (2005), First $^{40}Ar/^{39}Ar$ geochronology of
603 lateritic manganiferous pisolites: Implications for the palaeogene history of a West African
604 landscape, *Earth Planet. Sci. Letters*, *238*, 172-188.
605 Collins, D.N., A.R. Tron, J.C. Wilson, and P. Parsonage (1971), The treatment of Tambao
606 Manganese Ore deposit for United Nations, *Unpublished report*, 24pp., Warren Spring
607 Laboratory, Department of trade and industry, CR504.
608 Dasgupta, S., S. Roy, and M. Fukuoka (1992), Depositional models for manganese oxides
609 and carbonates deposits of the Precambrian Sausar group, India, *Econ. Geol.*, *87*(5), 1412-
610 1418.
611 Delfour, J. (1963), Géologie du gîte de manganese de Tambao (haute-Volta), *Unpublished*
612 *BRGM report 5612*, 20 pp., BRGM, Orléans, France.

613 Faure, H. (1966), Reconnaissance géologique des formations sédimentaires post-
614 paléozoïques du Niger oriental, Doct sci. Thesis, Univ. Paris, Mém. B.R.G.M., 47,
615 Orléans, France.
616 Flower, B.P., and J.P. Kennett (1994), The middle Miocene climatic transition: East
617 antarctic ice sheet development, deep ocean circulation and global carbon cycling, *Science*,
618 *108*(3/4), 537-555.
619 Gavaud, M. (1977), Les grands traits de la pédogenèse au Niger méridional, Travaux et
620 Documents ORSTOM, 76, 104 pp., Paris, France.
621 Grandin, G. (1976), Aplanissements cuirassés et enrichissement des gisements de
622 manganèse dans quelques régions d'Afrique de l'Ouest, Doct sci. thesis, Univ. Strasbourg,
623 Mém. ORSTOM, 82, Paris, France.
624 Gunnell, Y. (2003), radiometric ages of laterites and constraints on long-term denudation
625 rates in West Africa, *Geology*, *31*(2), 131-134.
626 Hall, C.M., R.C. Walter, J.A. Westgate, and D. York (1984), Geochronology, stratigraphy
627 and geochemistry of Cindery tuff in Pliocene hominid-bearing sediments of the middle
628 Awash, Ethiopia, *Nature*, *308*, 26-31.
629 Hautmann, S., and H.J. Lippolt (2000), $^{40}Ar/^{39}Ar$ dating of central European K-Mn oxides a
630 chronological framework of supergene alteration processes during the Neogene, *Chem.*
631 *Geol.*, *170*(1-4), 37-80.
632 Hénocque, O., G. Ruffet, F. Colin, and G. Féraud (1998), $^{40}Ar/^{39}Ar$ dating of West African
633 lateritic cryptomelanes, *Geochim. Cosmochim. Acta*, *62*(16), 2739-2756.
634 Kennett, J.P., and N.J. Shackleton (1976), Oxygen isotopic evidence for the development of
635 the psychrosphere 38 Ma ago, *Science*, *260*, 513-515.
636 King, L.C. (1967), *The morphology of the Earth. A study and synthesis of world scenery*,
637 2nd ed., Olivier & Boyd, Edinburgh, Scottland.

638 Lang, J., C. Kogbe, S. Alidou, K. A. Alzouma, G. Bellion, D. Dubois, A. Durand, R.
639 Guiraud, A. Houessou, I. de Klasz, E. Romann, M. Salard-Cheboldaeff, and J. Trichet
640 (1990), The continental terminal of West Africa, *J. Afr. Earth Sci.*, *10*(1-2), 79-99.
641 Lawver, L.A., L.M. Gahagan, and M.F. Coffin (1992), The development of paleoseaways
642 around Antarctica, in *The Antarctic Paleoenvironment: A perspective on global change*,
643 edited by L.P. Kennett and D.A. Warnke, pp. 7-30, Antarctic Research Series, 56.
644 Lippolt, H.J., and S. Hautmann (1995), $^{40}Ar/^{39}Ar$ ages of Precambrian manganese ore
645 minerals from Sweden, India and Morocco, *Miner. Deposita*, *30*, 246-256.
646 Ly, A. (1985), Le Tertiaire de Casamance (Sénégal) : Biostratigraphie (Foraminifères) et
647 sédimentologie d'après les données de subsurface, Doct. sci. Thesis, 215 pp., Univ. Aix-
648 Marseille III, Marseille, France.
649 Ly, A., and R. Anglada (1991), Le Bassin Sénégalo-Mauritanien dans l'évolution des marges
650 périatlantiques au Tertiaire, *Cahiers de Micropaléontologie*, *6*, 2, 23- 40.
651 Michel, P. (1973), Les Bassins des fleuves Sénégal et Gambie : étude géomorphologique,
652 Doct sci. Thesis, Univ. Strasbourg, Mém. ORSTOM, 63, Paris, France.
653 Michel, P. (1978), Cuirasses bauxitiques et ferrugineuses d'Afrique Occidentale Aperçu
654 chronologique, *Trav. Doc. Géogr. Trop.*, *33*, pp. 11-32, CEGET CNRS, Bordeaux, France.
655 Miller, K. G., M. A. Kominz, J. V. Browning, J. D. Wright, G. S. Mountain, M. E. Katz, P.
656 J. Sugaman, B. S. Cramer, N. Christie-Blick, and S. F. Pekar (2005), The phanerozoic
657 record of global sea-level change, *Science*, *310*, 1293-1298.
658 Millot, G. (1970), *Geology of clays*, Chapman and Hall, London.
659 Millot, G. (1983), Planation of continents by intertropical weathering and pedogenetic
660 processes, in *lateritisation processes*, pp. 53-63, edited by A. J. Melfi and A. Carvalho,
661 Proceedings of the II$^{nd}$ international Seminar on Lateritisation Processes, Sao Paulo, Brazil.

662 Nahon, D. (1991), *Introduction to the petrology of soils and chemical weathering*, John
663 Wiley and sons, New York.
664 Nahon, D., A. Beauvais, P. Nziengui-Mapangou, and J. Ducloux (1984), Chemical
665 weathering of Mn-garnets under lateritic conditions in northwest Ivory Coast (West
666 Africa), *Chem. Geol.*, *45*, 53-71.
667 Nahon, D., B. Boulangé, and F. Colin (1992), Metallogeny of weathering: an introduction, in
668 *Weathering, soils & paleosols*, pp. 445-467, edited by I.P. Martini and W. Chesworth,
669 Developments in Earth Surface Processes 2, Elsevier, Amsterdam.
670 Oswald, J. (1992), Genesis and paragenesis of the tretravalent manganese oxides of the
671 australian continent, *Econ. Geol.*, *87*(5), 1237-1253.
672 Parc S., D. Nahon, Y. Tardy, and P. Vieillard (1989), Estimated solubility products and field
673 of stability for cryptomelane, nsutite, birnessite and lithiophorite based on natural lateritic
674 weathering sequences, *Amer. Miner.*, *74*, 466-475.
675 Partridge, T.C., and R.R. Maud (1987), Geomorphic evolution of Southern Africa since the
676 Mesozoic, *S. Afr. J. Geol.*, *90*, 179-208.
677 Pedro, G. (1968), Distribution des principaux types d'altération chimique à la surface du
678 globe, *Rev. Géogr. Phys. Géol. Dyn.*, *10*(5), 457-470.
679 Perseil E.A., and G. Grandin (1978), Evolution minéralogique du manganèse dans trois
680 gisements d'Afrique de l'Ouest : Mokta, Tambao, Nsuta. *Miner. Deposita*, *13*, 295-311.
681 Petters S.W. (1977), Ancient Seaway across the Sahara, *Nigerian Field*, *42*, 23-31.
682 Picot P., and R. Trinquard (1969), La manganosite (MnO) du gîte de manganèse de Tambao
683 (Haute-Volta), *Bull. Soc. fr. Minér. Cristallogr.*, *92*, 500-502.
684 Pracejus B., and B.R. Bolton (1992), Geochemistry of supergene manganese oxide deposits,
685 Groote Eylandt, Australia, *Econ. Geol.*, *87*(5), 1310-1335.

686 Retallack G.J., J.G Wynn, and T.J. Fremd (2004), Glacial-interglacial-scale paleoclimatic
687 change without large ice sheets in the Oligocene of central Oregon, *Geology*, 32(4), 297-
688 300.
689 Roddick J. C. (1983), High precision intercalibration of $^{40}Ar/^{39}Ar$ standards. *Geochim.*
690 *Cosmochim. Acta*, *47*, 887-898.
691 Roy S. (1981), *Manganese deposits*, Academic press, London.
692 Roy S. (1988), Manganese metallogenesis : a review, *Ore Geol. Rev.*, *4*(1-2), 155-170.
693 Ruffet G., C. Innocent, A. Michard, G. Féraud, A. Beauvais, D. Nahon, and B. Hamelin
694 (1996), A geochronological $^{40}Ar/^{39}Ar$ and $^{87}Rb/^{87}Sr$ study of K-Mn oxides from the
695 weathering sequence of Azul (Brazil), *Geochim. Cosmochim. Acta*, *60*, 2219-2232.
696 Salamy K.A., and J.C. Zachos (1999), Latest Eocene-Early Oligocene climate change and
697 Southern Ocean fertility : inferences from sediment accumulation and stable isotope data,
698 *Pal. Pal. Pal.*, *145*, 61-77.
699 Segev A., L. Halicz, B. Lang, and G. Steinitz (1991), K-Ar dating of manganese minerals
700 from the Eisenbach region, Black Forest, Southwest Germany, *Schweiz. Mineral. Petrogr.*
701 *Mitt.*, *71*, 101-114.
702 Tardy Y., and C. Roquin (1998), *Dérive des continents, paléoclimays et altérations*
703 *tropicales*, BRGM, Orléans, France.
704 Thomas, M.F. (1994), *Geomoprhology in the tropics. A study of weathering and denudation*
705 *in low latitudes*, Wiley, New York.
706 Turner G. (1971), $^{40}Ar$-$^{39}Ar$ ages from the lunar maria, *Earth Planet. Sci. Lett.*, *11*, 169-191.
707 Turner G., and P.H. Cadogan (1974). Possible effects of $^{39}Ar$ recoil in $^{40}Ar$-$^{39}Ar$ dating, paper
708 presented at 5th lunar Conference, 2, 1601-1615.
709 Turner S., and P.R. Buseck (1979), Manganese Oxide Tunnel Structures and their
710 Intergrowths, *Science*, *203*, 456-458.

711 Varentsov I.M., and D.I. Golovin (1987), Groote Eylandt Manganese deposit, North
712 Australia : K-Ar age of cryptomelane ores and aspects of genesis, *Reports Acad. Sci.*
713 USSR, 294(1), 203-207.
714 Varentsov I.M. (1996), *Manganese ores of supergene zone : geochemistry of formation*,
715 Kluwer Academic Publisher, Dordrecht, The Netherlands.
716 Vasconcelos P.M. (1999), K-Ar and $^{40}Ar/^{39}Ar$ geochronology of weathering processes, *Annu.*
717 *Rev. Earth Planet. Sci.*, *27*, 183-229.
718 Vasconcelos P.M., T.A. Becker, P.R. Renne, and G.H. Brimhall (1992), Age and duration of
719 weathering by $^{40}K$-$^{40}Ar$ and $^{40}Ar/^{39}Ar$ analysis of Potassium-Manganese Oxides, *Science*,
720 *58*, 451-455.
721 Vasconcelos P.M., P.R. Renne, T.A. Becker, and H.R. Wenk (1995), Mechanisms and
722 kinetics of atmospheric, radiogenic, and nucleogenic argon release from cryptomelane
723 during $^{40}Ar/^{39}Ar$ analysis, *Geochim. Cosmochim. Acta*, *59*(10), 2057-2070.
724 Vasconcelos P.M., P.R. Renne, G.H. Brimhall, and T.A. Becker (1994), Direct dating of
725 weathering phenomena by $^{40}Ar/^{39}Ar$ and K-Ar analysis of supergene K-Mn oxides,
726 *Geochim. Cosmochim. Acta*, *58*, 1635-1665.
727 Vogt, J. (1959), Aspects de l'évolution géomorphologique récente de l'Ouest africain, *Ann.*
728 *Géogr. Fr.*, *68*(367), 193-206.
729 Yashvili L.P., and R.K. Gukasyan (1974), Use of cryptomelane for potassium-argon dating
730 of manganese ore of the Sevkar-Sargyukh deposit, Armenia, *Doklady Earth Sci. Sect.*, *212*,
731 49-51.
732 Zachos J.C., M. Pagani, L. Sloan, E. Thomas, and K. Billups (2001), Trends, rhythms, and
733 aberrations in global climate 65 Ma to present, *Science*, 292, 686-693.

734 Zachos J.C., T.M. Quinn, and K.A. Salamy (1996), High-resolution (104 years) deep-sea
735 foraminiferal stable isotope records of the Eocene-Oligocene climate transition,
736 *Paleoceanography*, *11*(3), 251-266.
737 Zachos J.C., L.D. Stott, and K.C. Lohmann (1994), Evolution of early Cenozoïque marine
738 temperatures, *Paleoceanography*, *9*(2), 353-387.
739 Zartman R. E. (1964), A geochronological study of the Love Grove Pluton from the Llano
740 uplift, Texas, *Journal of Petrology*, *5*, 359-408.
741

741 **Figures caption**

742
743 Figure 1. Synthetic geomorphological sequence of lateritic paleolandsurfaces in West Africa
744 (The rectangle defines the Tambao sequence in North Burkina Faso).

745
746 Figure 2. Location and geomorphologic patterns of the Mn-ore deposit of Tambao in North
747 Burkina Faso, with the locations of the drill cores, and a section (A-B) across the main
748 geological formations (blue circle in the inset = intracratonic sedimentary basin).

749
750 Figure 3. Logs of the drill cores with the locations of samples dated by the $^{39}Ar$-$^{40}Ar$ method.

751
752 Figure 4. (a) SEM photomicrograph of cryptomelane needles with (b) its chemical analysis.

753
754 Figure 5. Photomicrographs of (a) cryptomelane (C) vein, (b) cryptomelane (C) developing
755 from the metasomatism of pyrolusiste (P), and (c) botryoidal cryptomelane.

756
757 Figure 6. Geochemical evolution along DD2B drill core.

758
759 Figure 7. $^{39}Ar$-$^{40}Ar$ age spectra configuration, (a) Type 1 (stair case), (b) Type 2 (hump) shape
760 and (c) Type 3. (ca. = concordant apparent ages)

761
762 Figure 8. $^{39}Ar$-$^{40}Ar$ age spectra of cyptomelane extracted from the upper part of the deposit
763 (342-325 m altitudes), (a) outcrop and intermediate surface samples, (b) DDH76-02 drill
764 core, (c) DD2B drill core, and (d) frequency diagram of apparent ages. (See figure 3 for
765 sample locations).

766
767 Figure 9. $^{39}Ar$-$^{40}Ar$ age spectra of cyptomelane extracted from the upper and middle parts of
768 the deposit (325-300 m altitudes), (a) outcrop samples, (b) and (c) DD2B drill core, (d)
769 DDH76-02 drill core, (e) and (f) DDH76-09 drill core, and (g) frequency diagram of
770 apparent ages. (See figure 3 for sample locations).

771 Figure 10. $^{39}Ar$-$^{40}Ar$ age spectra of cyptomelane extracted from the lower part of the deposit
772 (300-253 altitudes), (a) samples from DD2B, DDH76-09 drill cores and low glacis (b)
773 DDH76-02 drill core, and (c) frequency diagram of apparent ages. (See figure 3 for sample
774 locations).

775
776 Figure 11. (a) Distribution of pseudo-plateau and plateau ages as a function of altitude in the
777 Mn-deposit with the superimposition of the elevation ranges of each landsurface (b) 3D
778 frequency diagram of all apparent ages versus altitude. (Curved black arrow = decreasing
779 chemical weathering and increasing erosion rate).

780
781 Figure 12. Comparison between the global curves of (a) $\delta^{18}O$-paleotemperatures and (b)
782 eustatic levels, both from *Miller et al.* [2005], with (c) $^{39}Ar$-$^{40}Ar$ age groups (grey scale
783 bands) defined by pseudo-plateau or plateau ages depicted in this work. (The dotted grey
784 curve in (b) is the long term fit of the sea level curve and the straight dotted black segments
785 represent the erosion periods; the rectangle and dotted rectangles in (c) represents the $^{39}Ar$-
786 $^{40}Ar$ age groups previously obtained by *Henocque et al.* [1998] and *Colin et al.* [2005],
787 respectively; the dark grey histogram in (c) represents the age frequency weighted by the
788 error margin for the deposit as a whole; the light grey scale band represents the paroxysm of
789 the bauxitic weathering period).

790
791 Figure 13. (a) Geomorphological relationships between the lateritic paleolandsurfaces (dotted
792 lines) and the sedimentary sequences of the Iullemmeden basin of Niger in West Africa (the
793 light grey trapezoids represent the denuded bauxites and the vertical black arrow represents
794 the total denudation of the regolith. (b) Detailed morphogenetic processes around Tambao
795 (black numbers = weathering periods in Ma; grey numbers = erosion periods in Ma; vertical
796 grey arrows = regolith denudation and topographic decay).

797

797

798

799

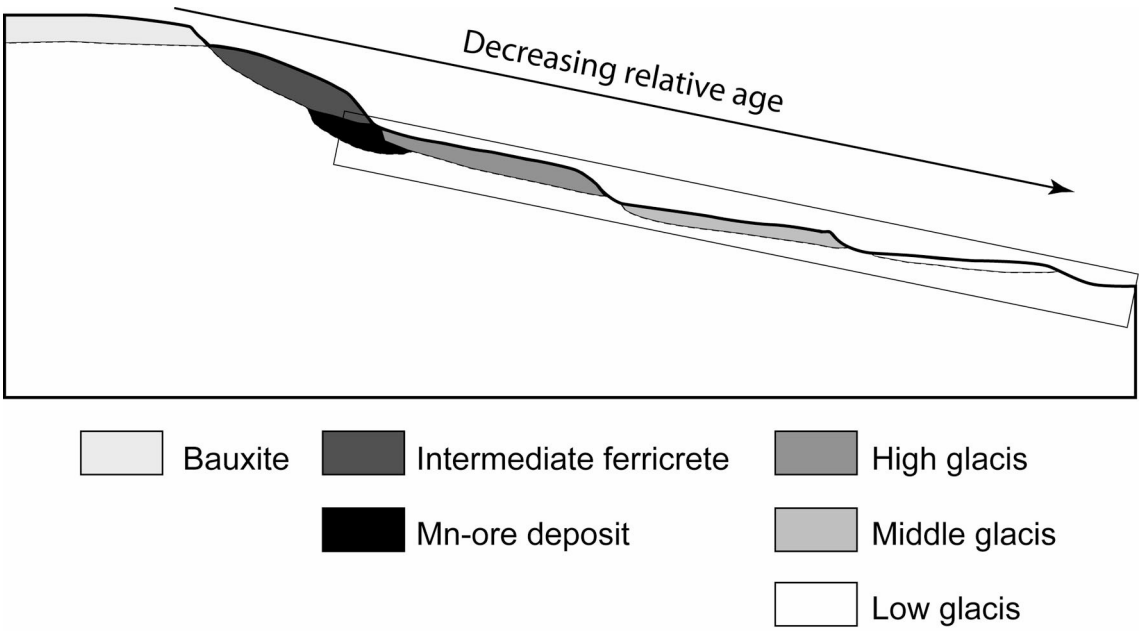


Fig. 1

800 *Beauvais et al., 2008*

801

801

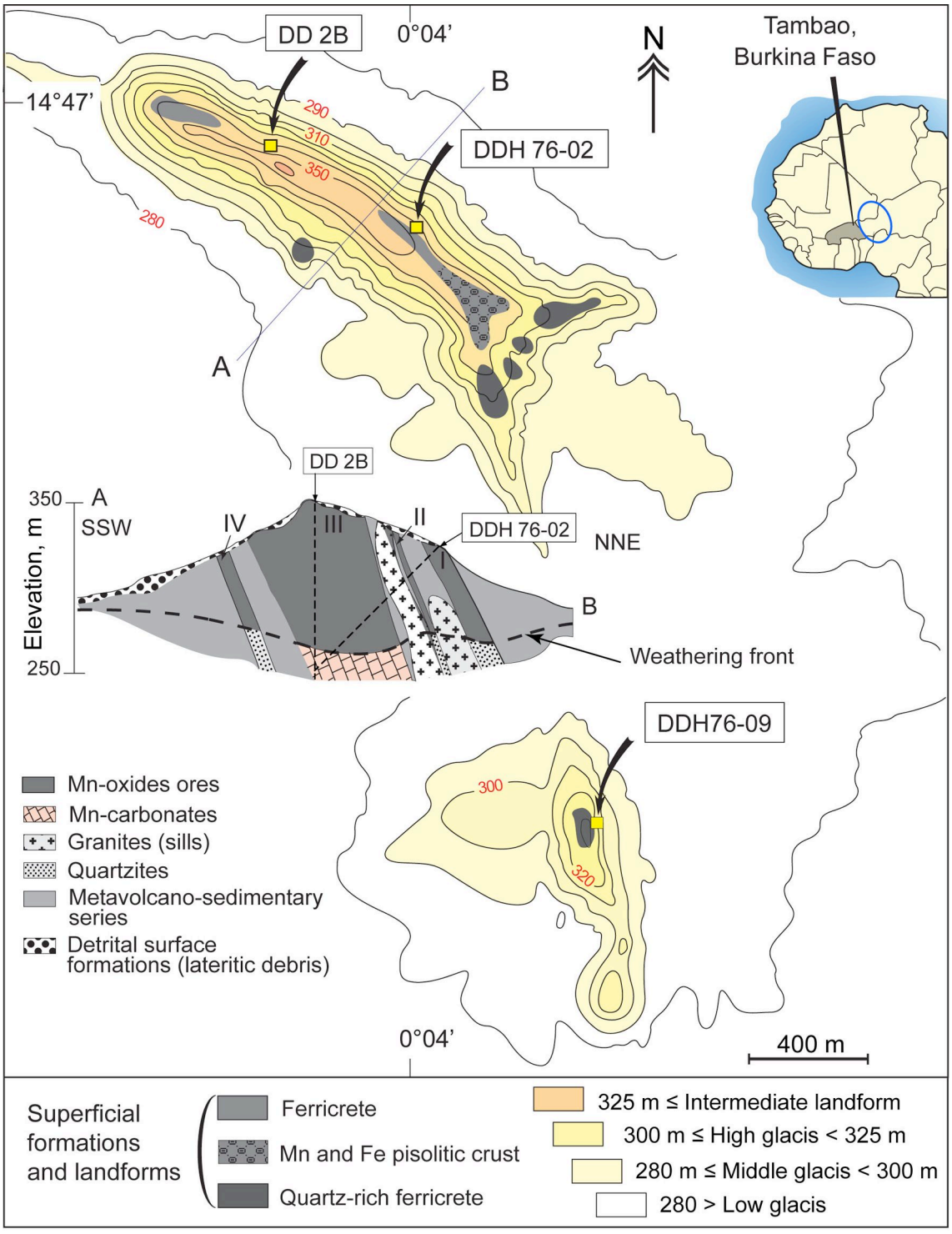


Fig. 2

802 *Beauvais et al., 2008*

803

803

804

805

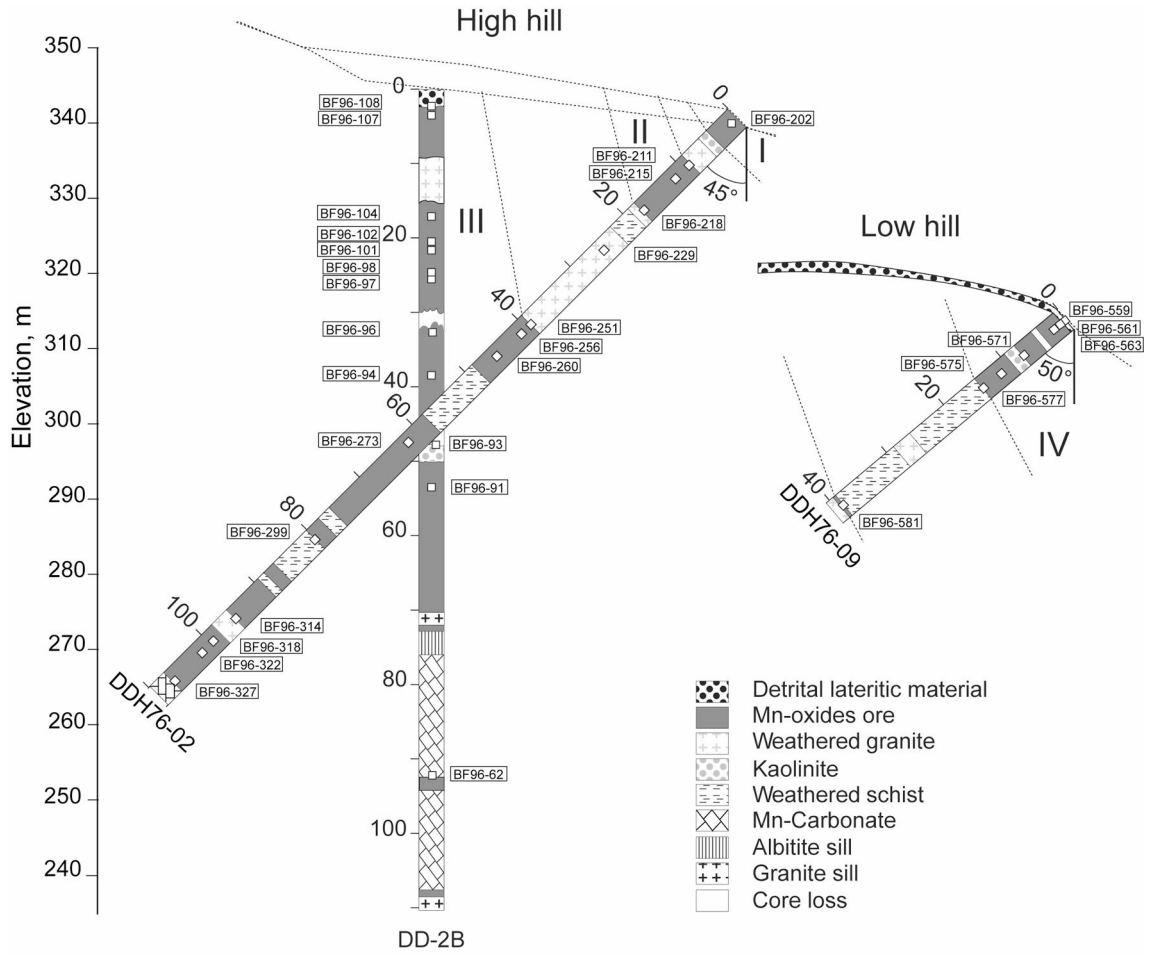


Fig.3

806 *Beauvais et al., 2008*

807

807

808

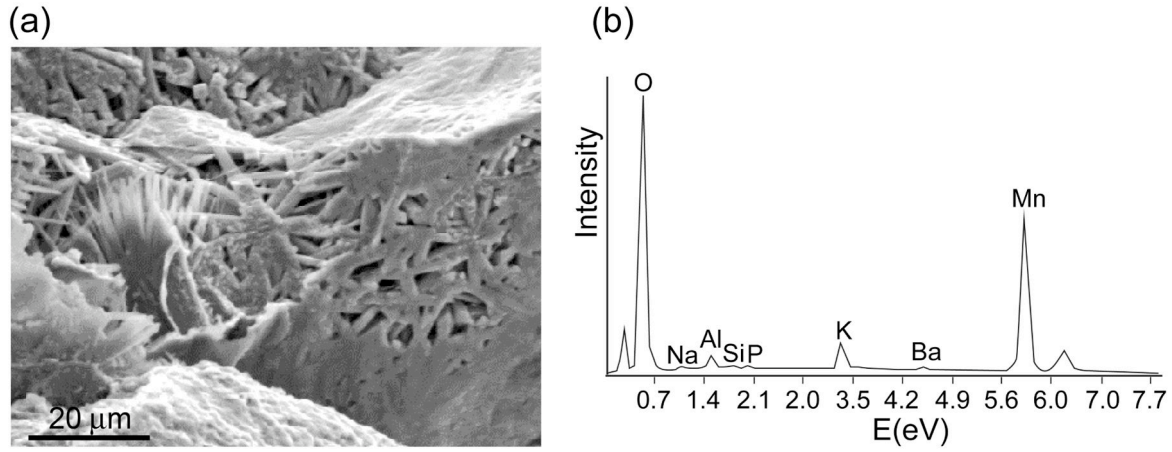


809 Fig. 4 *Beauvais et al., 2008*

810

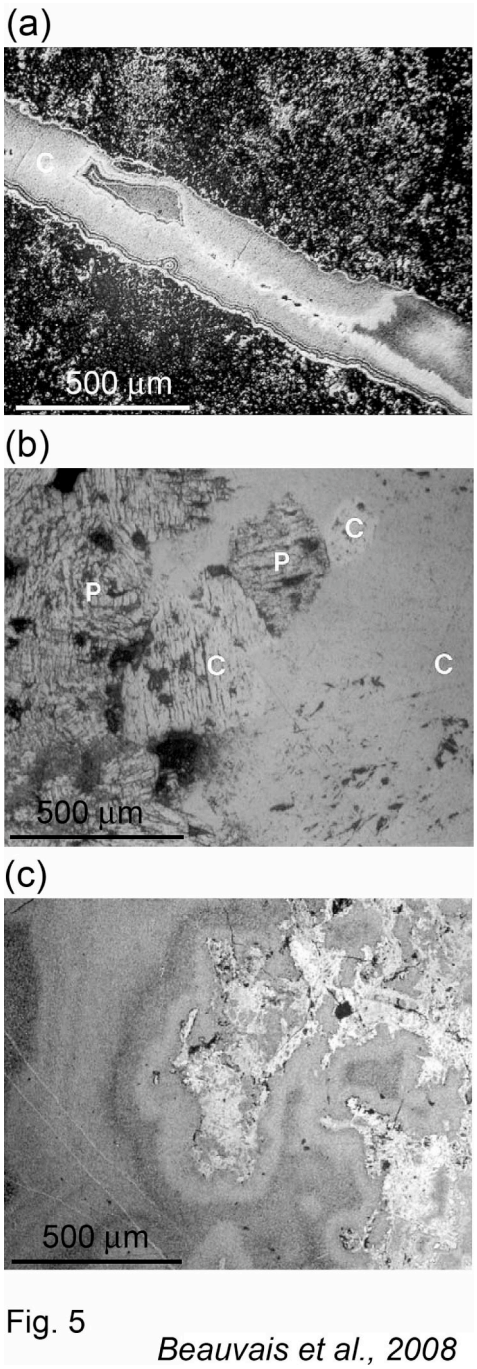


Fig. 5 *Beauvais et al., 2008*

812

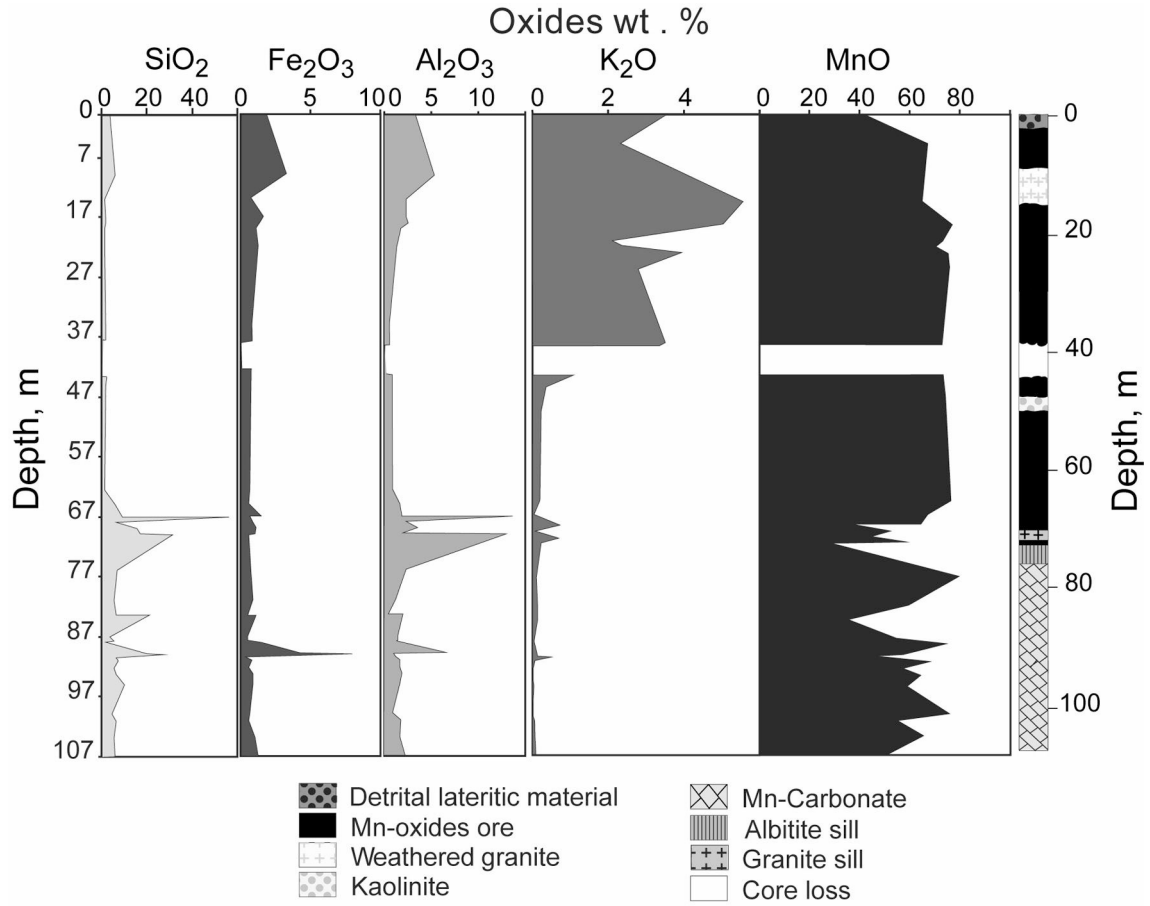


Fig. 6

813 *Beauvais et al., 2008*

814

814

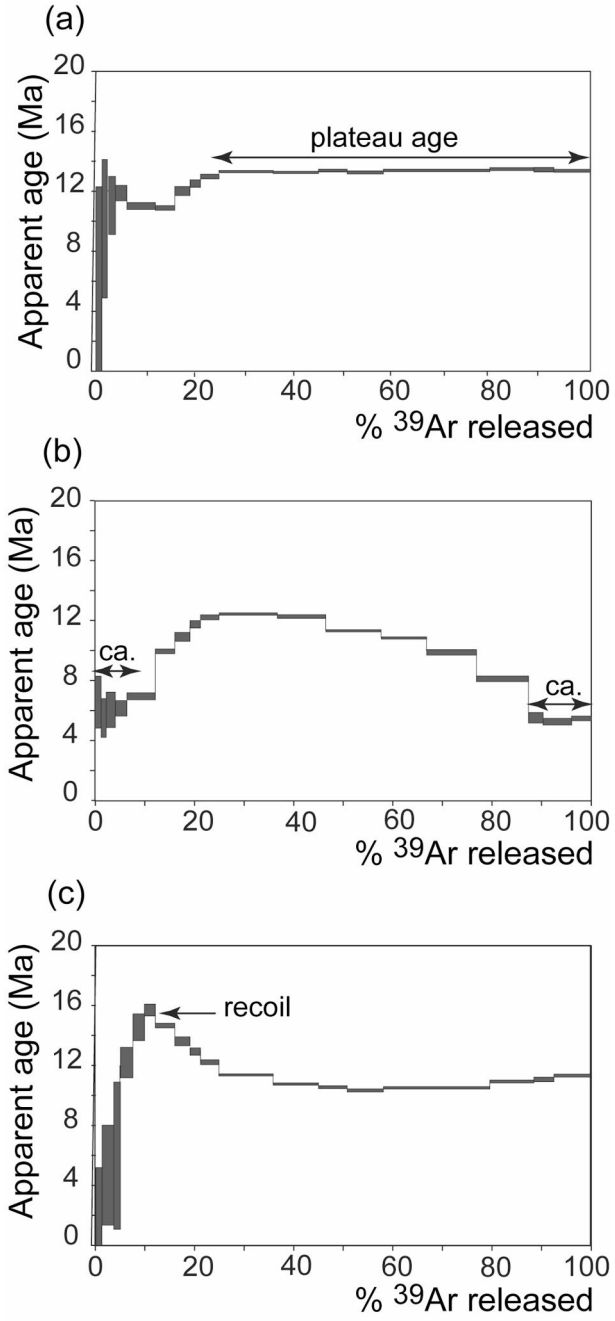


Fig. 7

815 *Beauvais et al., 2008*

816

816

817

818

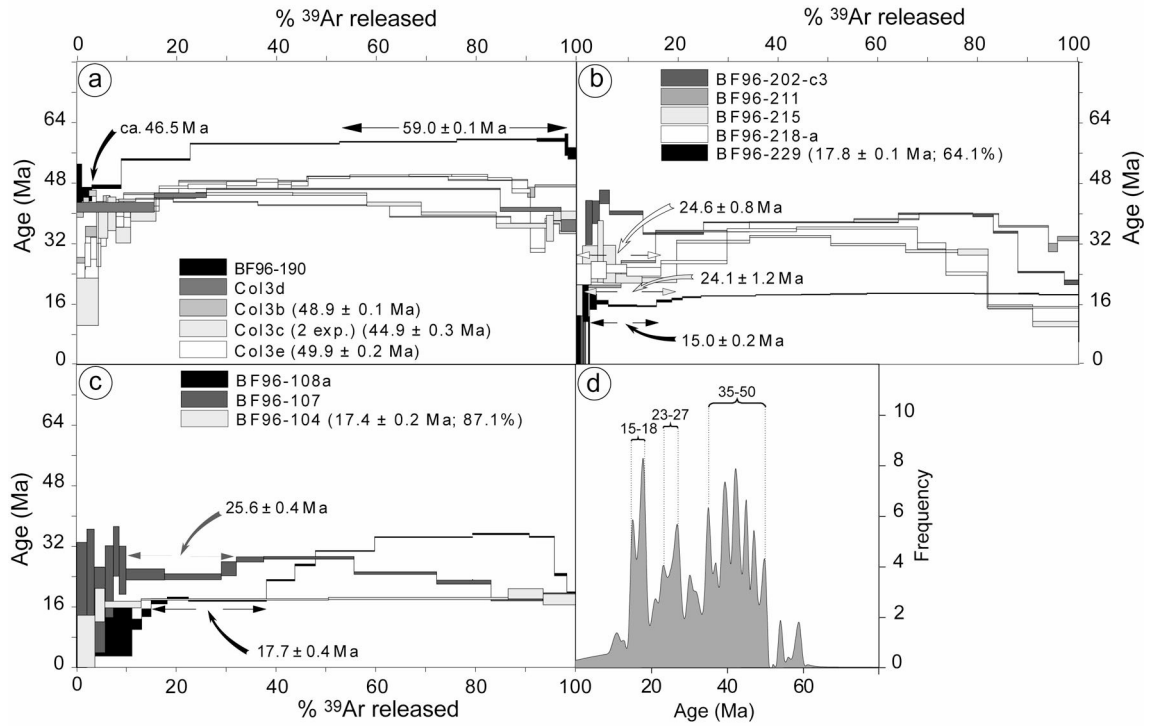


Figure 8

819 *Beauvais et al., 2008*

820

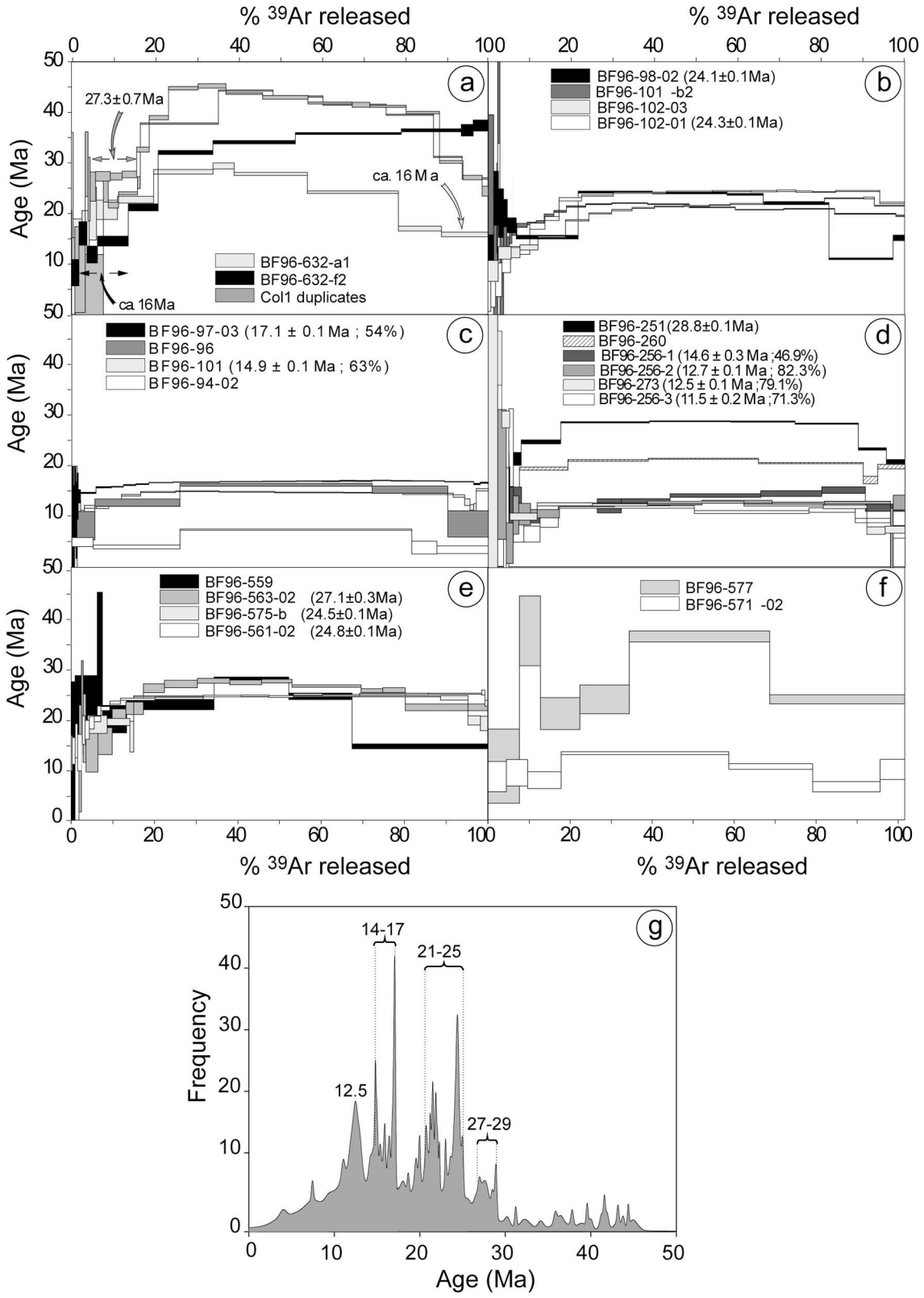


Figure 9

820 *Beauvais et al., 2008*

821

821

822

823

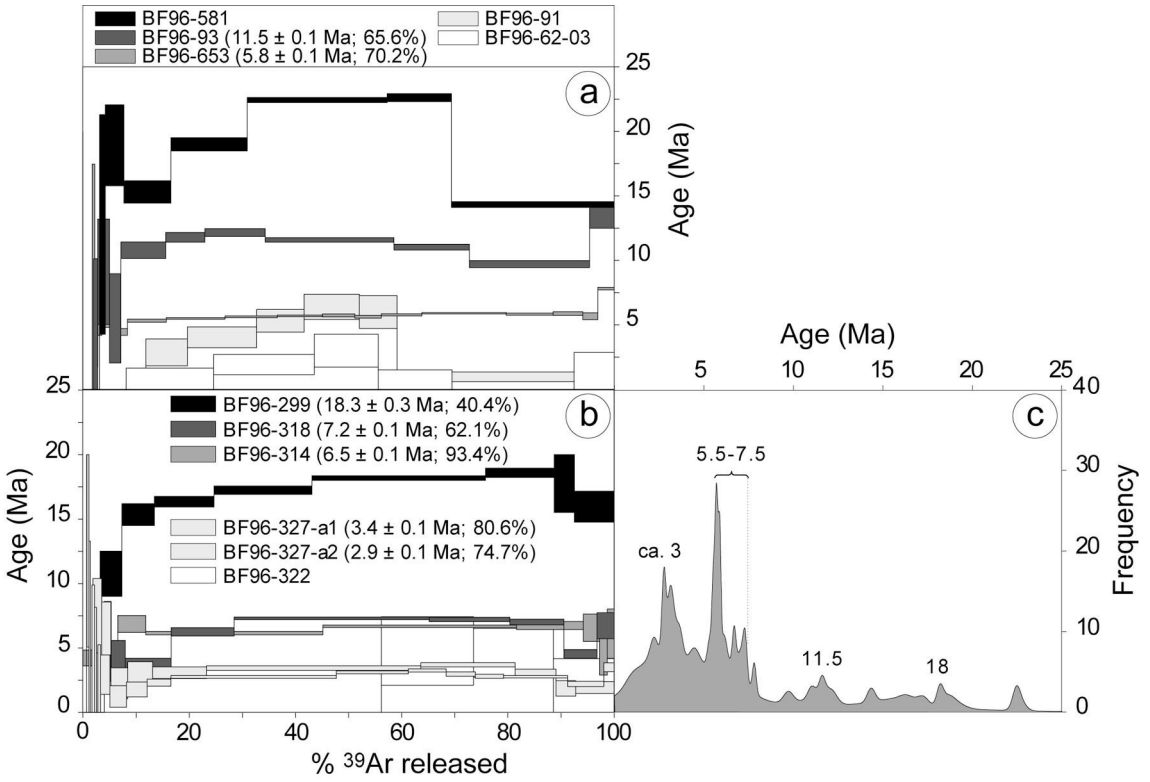


Figure 10

824 *Beauvais et al., 2008*

825

825

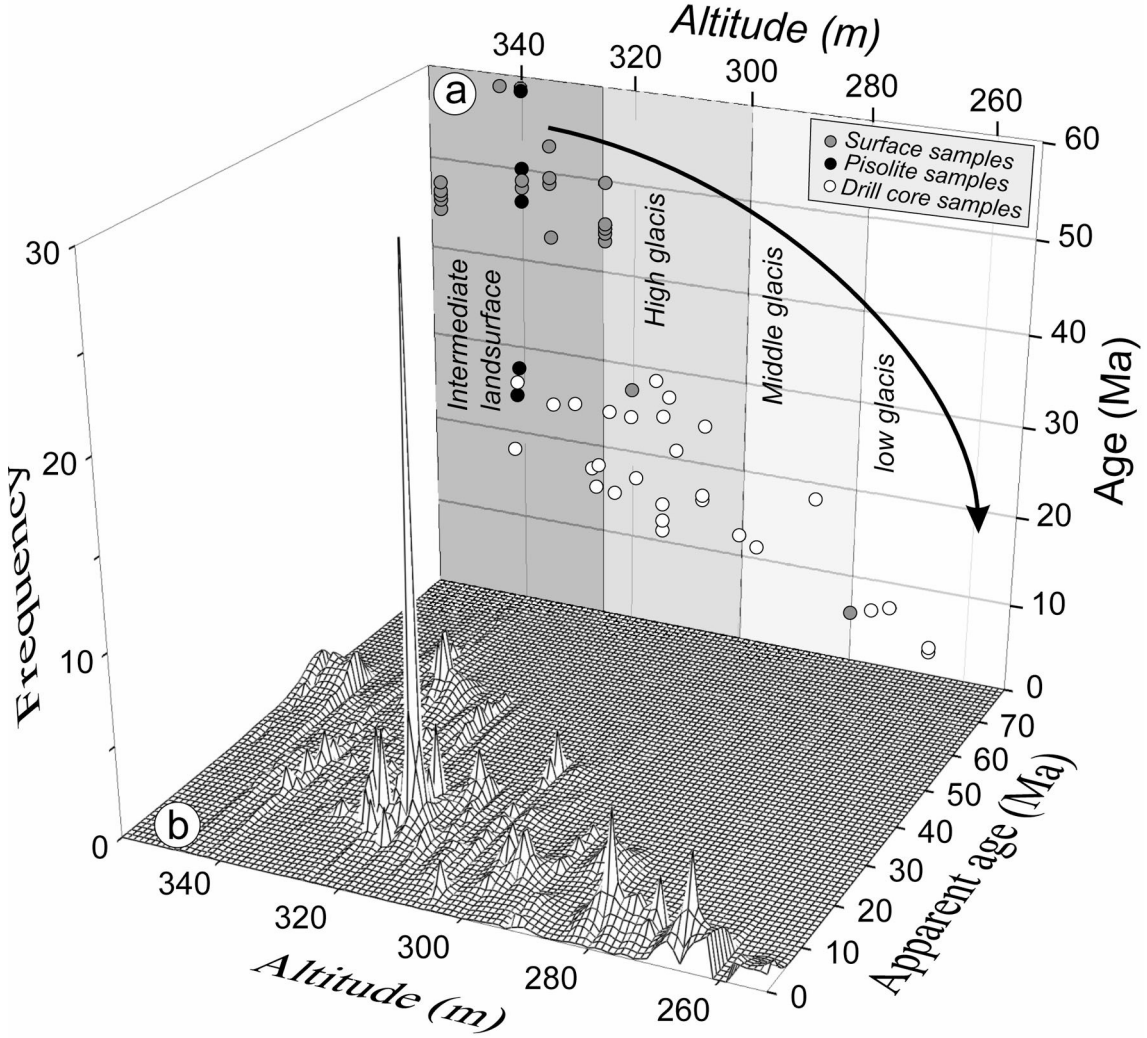


FIG. 11

826 *Beauvais et al., 2008*

827

827

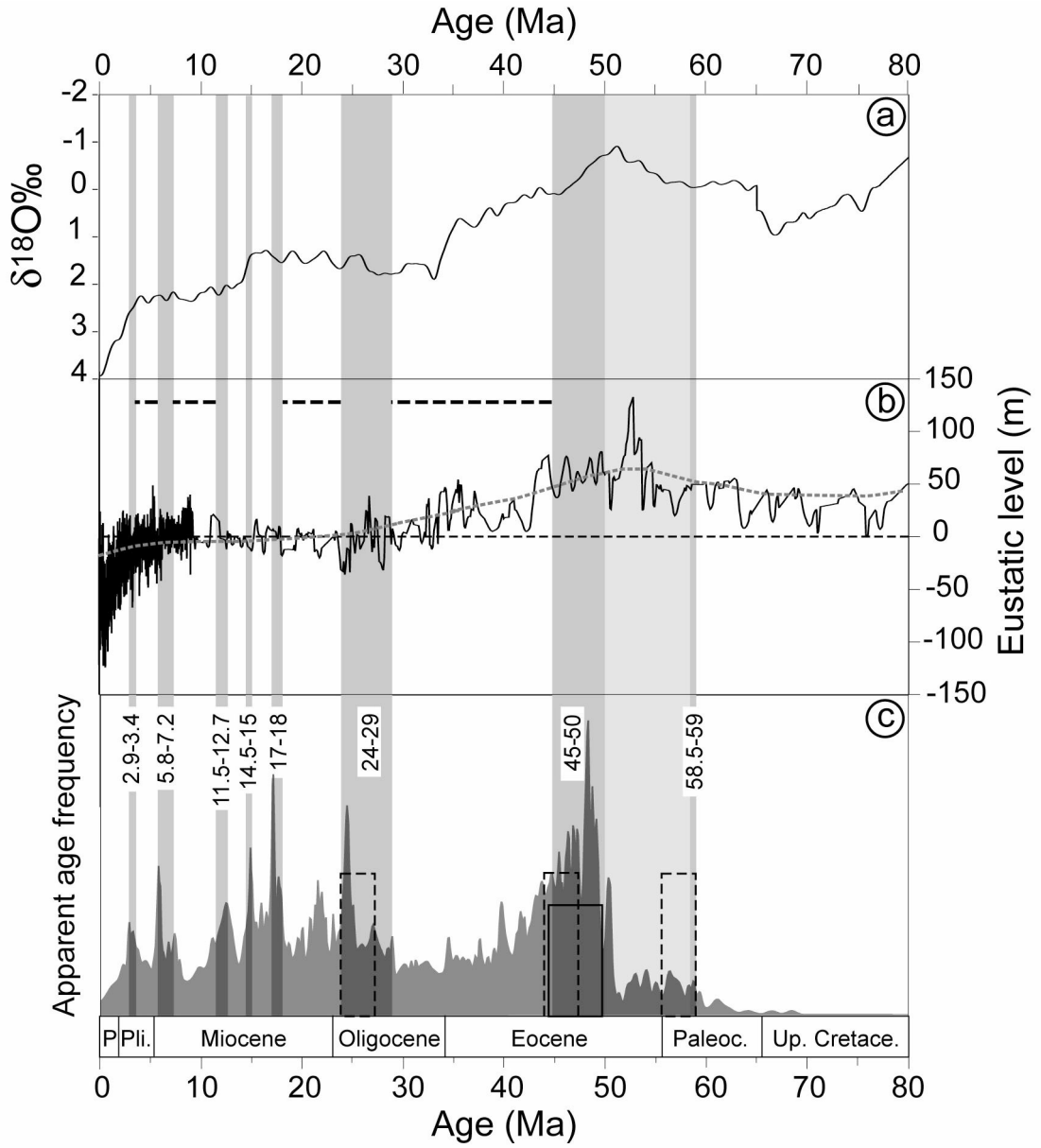


FIG. 12

*Beauvais et al., 2008*

828

829

829

830

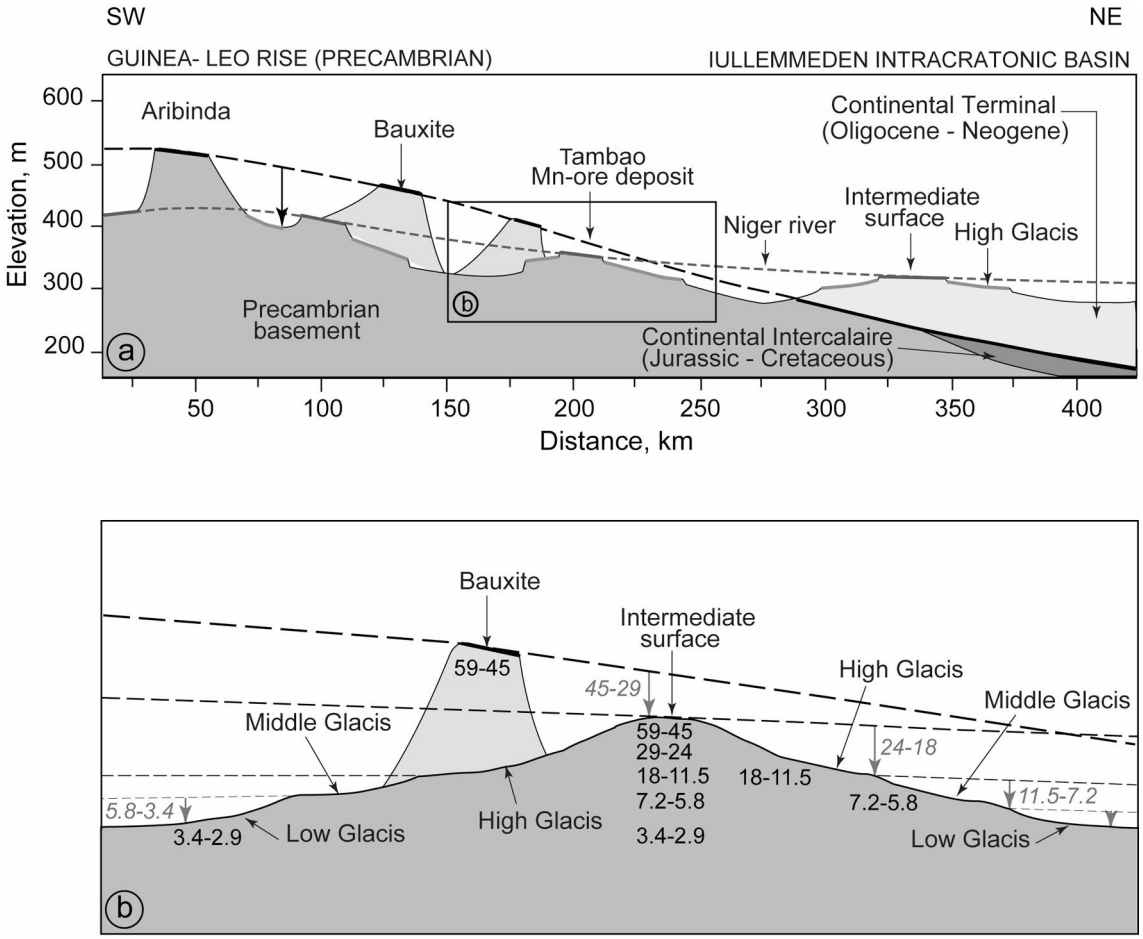


Figure 13

831 *Beauvais et al., 2008*